The SET1/COMPASS subunit RBBP5 orchestrates epigenetic control of global proteostasis and the 12h oscillator to safeguard metabolic and cellular homeostasis

Syeda Kubra[1, #], Michelle Sun[1, #], William Dion[1], Ahmet Catak[1], Hannah Luong[1], Haokun Wang[1], Yinghong Pan[2, ¥], Jia-Jun Liu[3,4], Aishwarya Ponna[1], Lijun Liu [3,5], Ian Sipula[6], Jian-Hua Luo [3,5], Michael J. Jurczak[6,7], Silvia Liu[3,4,8], and Bokai Zhu[1,3,6] *

[1] Aging Institute of UPMC, University of Pittsburgh School of Medicine, Pittsburgh, PA, U.S.A.

[2] UPMC Genome Center, UPMC, Pittsburgh, PA, U.S.A.

[3] Pittsburgh Liver Research Center, University of Pittsburgh, Pittsburgh, PA, U.S.A.

[4] Organ Pathobiology and Therapeutics Institute, University of Pittsburgh School of Medicine, Pittsburgh, PA, U.S.A.

[5] Department of Pathology, University of Pittsburgh School of Medicine, Pittsburgh, PA, U.S.A.

[6] Division of Endocrinology and Metabolism, Department of Medicine, University of Pittsburgh School of Medicine, Pittsburgh, PA, U.S.A.

[7] Center for Metabolism and Mitochondrial Medicine, University of Pittsburgh School of Medicine, Pittsburgh, PA, U.S.A.

[8] Department of Pharmacology and Chemical Biology, University of Pittsburgh School of Medicine, Pittsburgh, PA, U.S.A.

# These authors contribute equally.

¥ Present address: UPMC Magee-Womens Hospital, Pittsburgh, PA, U.S.A.

* Corresponding author: Bokai Zhu: bzhu@pitt.edu

One sentence summary:

RBBP5 regulates global mammalian proteostasis.

Abstract:

Proteostasis is vital for cellular health, with disruptions leading to aging, neurodegeneration and metabolic disorders. Traditionally, proteotoxic stress responses were studied as acute reactions to various noxious factors; however, recent evidence reveals that many proteostasis genes exhibit ~12h ultradian rhythms under physiological conditions in mammals, driven by an XBP1s-dependent 12h oscillator. By examining the chromatin landscape of this oscillator, we identified RBBP5 as an essential epigenetic regulator of global proteostasis dynamics. Mechanistically, as the core subunit of the SET1/COMPASS complex, RBBP5 co-activates XBP1s to facilitate dynamic proteostasis gene expression by marking promoter-proximal H3K4me3, which further recruits the Integrator Complex and SWI/SNF chromatin remodelers. Functionally, RBBP5 is indispensable for regulating both the 12h oscillator and acute transcriptional response to various proteotoxic stresses, including ER stress and nutrient deprivation. RBBP5 ablation causes increased susceptibility to proteotoxic stress, chronic inflammation, and hepatic steatosis in mice, along with impaired autophagy and reduced cell survival *in vitro*. In humans, lower *RBBP5* expression is associated with reduced adaptive stress-response gene expression and hepatic steatosis. Our findings not only highlight a previously unrecognized epigenetic timing mechanism distinct from circadian regulation but also establish RBBP5 as a central regulator of proteostasis, essential for cellular resilience and organismal health.

Introduction:

Proteostasis, the maintenance of proper protein folding, trafficking, and turnover, is a major challenge for the cell (1). Much of the cellular energy expenditure is dedicated to maintaining a healthy proteome, as millions of molecules are produced every single minute (2). Challenges to proteostasis, exemplified by the accumulation of unfolded or misfolded proteins, can lead to a range of cellular dysfunctions and pathological conditions, such as aging, neurodegenerative diseases, cancer, and metabolic disorders (1,3-6). To cope with proteotoxic stress, organisms have developed a wide range of stress response mechanisms, including the heat shock response, the unfolded protein response (UPR), and the more generalized integrated stress response (ISR) (7-9). Although the detailed signaling molecules vary, these pathways generally involve transmitting the information of cellular stress to the nucleus by activating various transcription factors (TF) containing the basic leucine zipper domain (bZIP), such as spliced form of XBP1 (XBP1s), ATF4 and ATF6 and heat shock factor 1 (HSF1). After binding the stress response element in the promoters/enhancers, these TFs in turn upregulate a plethora of genes aimed to restore proteostasis (10,11).

While proteotoxic stress responses were traditionally viewed and studied as distinct acute responses to different “noxious” factors, recent evidence by our group indicates that at the physiological level (and in the absence of evident extrinsic stress), the expression of hundreds of proteotoxic stress response regulatory and output genes exhibit cell-autonomous ultradian rhythms cycling with a ~12h period in multiple mammalian cell-types and tissues, including humans (12-21). These proteostasis genes encompass both output genes involved in protein processing in the ER/Golgi, redox regulation, protein folding, ER-associated protein degradation (ERAD), autophagy, and upstream regulatory molecules and TFs like *Xbp1*, *Atf4*, *Atf6*, *Ddit3*, *Perk* and *Ire1α* (12,22). Many of these ~12h ultradian rhythms are established by an XBP1s-dependent 12h ultradian oscillator separate from both the ~24h circadian clock and the cell cycle (21,23,24). It is hypothesized that the mammalian 12h oscillator may have evolved from the circatidal clock of marine animals, and later co-opted to adapt to the ~12h cycle of metabolic stress peaking at transition times at dawn and dusk in terrestrial animals (13,16,21,25). The 12h oscillator is well-studied in the liver, and mice with liver-specific 12h oscillator ablation exhibited accelerated liver aging and steatosis (19), manifested with impaired proteostasis, lipid metabolism, and

mitochondria dysfunction (19,20,26). Since the 12h oscillator integrates multiple proteotoxic stress signaling, it provides us with a unique opportunity to study proteostasis using a holistic approach: rather than studying individual stress response separately, by investigating the 12h oscillator we could gain new mechanistic insights for universal proteostasis regulation.

While significant work has been done on upstream proteotoxic stress sensing and protein-folding mechanisms in the ER and cytosol, there remains a lack of fundamental understanding of the transcriptional regulation of proteostasis in general, particularly concerning the temporal epigenome dynamics, chromatin landscapes, and co-regulatory networks underlying global proteostasis control. In this study, we seek to address an important unanswered question: is there a designated epigenetic regulator that orchestrates global proteostasis dynamics? By analyzing the chromatin landscape of the murine 12h hepatic oscillator, we identified RBBP5—an essential subunit of the Complex Proteins Associated with Set1 (COMPASS) complex responsible for depositing H3K4me3 (27) —as a pivotal epigenetic regulator that governs global proteostasis dynamics. By contrast, histone acetyltransferase (HAT) and associated H3K9Ac are dispensable for dynamic proteostasis gene expression. RBBP5 plays a critical role in regulating both the 12h oscillator and transcriptional response to a plethora of acute proteostasis stress, functioning as a co-activator for XBP1s, to mark H3K4me3 at the promoter of proteostasis genes. Proximity labeling of H3K4me3 further reveals the chromatin-associated proteomic architecture during proteostatic stress, including subunits of the Integrator complex and SWI/SNF chromatin remodelers. Loss of RBBP5 leads to heightened susceptibility to proteotoxic stress, driving chronic inflammation and hepatic steatosis in mice, while also impairing autophagy and cell survival *in vitro*. In humans, reduced RBBP5 expression is linked to a weakened adaptive stress response and the onset of hepatic steatosis. Our findings not only highlight a previously unrecognized epigenetic timing mechanism distinct from circadian regulation but also establish RBBP5 as a central regulator of proteostasis, essential for cellular resilience and organismal health.

Materials and Methods:

Plasmids

pCDH-EF1a-mCherry-EGFP-LC3B was a gift from Sang-Hun Lee (Addgene plasmid # 170446; http://n2t.net/addgene:170446; RRID: Addgene_170446) (28). pLenti-X1-hygro-mCherry-RAMP4 was a gift from Jacob Corn (Addgene plasmid # 118391; http://n2t.net/addgene:118391; RRID:Addgene_118391) (29).

The generation of *Rbbp5* $^{(flox/flox)}$ mice

The Rbbp5-flox allele was generated by the Mouse Embryo Services Core (University of Pittsburgh, Department of Immunology). The targeting strategy is based on the Easi-CRISPR method (30). In brief, fertilized embryos from C57BL/6J background, produced by natural mating, were microinjected in the pronuclei with a mixture of 0.67 μM EnGen Cas9 protein (New England Biolabs, Cat.No. M0646T), two Cas9 guides RNA: Rbbp5-695rev and Rbbp5-951forw (21.23 ng/μl each) and a long single stranded oligonucleotides Rbbp5-flox-ssODN (5 ng/μl). The long single stranded oligonucleotide encoding the donor sequence was synthesized by Integrated DNA Technologies (IDT).

To produce the sgRNA, a double strand linear DNA template is created by annealing of the following target specific oligonucleotides with a common primer (gRNA-Scaffold-R: 5'-AAAAAAGCACCGACTCGGTGCCACTTTTTCAAGTTGATAACGGACTAGCCTTATTTTAACTTGCTATTTCTAGCTCTAAAAC-3') containing the full tracrRNA sequence and then PCR amplified as

previously described (31). The sgRNA was synthesized using HiScribe T7 Quick High Yield RNA Synthesis Kit (New England Biolabs, Cat. No. E2050S).

T7-Rbbp5-695rev sequence:

TAATACGACTCACTATAGGAAGCATTCTAAGATTAAACCGTTTTAGAGCTAGAAATAGCA

T7-Rbbp5-951forw sequence:

TAATACGACTCACTATAGGAGTAACAGATAGTATTCCGAGTTTTAGAGCTAGAAATAGCA

Rbbp5-flox-ssODN sequence:

gcagttaataaacttgaagtgtttatatagaaaatacatcaggatggcaaccaaacccttttagatacctgagattttattctcttatcccag
gtATAACTTCGTATAGCATACATTATACGAAGTTATgaattcttaatcttagaatgcttagtctgtttcatgctgaagata
agttgtcagaactcacattgttactgatttttcgttcagtgactcgtctgttttgtcataggaaaattggagtgcatttgcaccagacttcaaag
agttggatgaaaatgtagaatatgaggaaagagaatcagaatttgatattgaggatgaagataagagtgagcctgagcaaacaggt
gatgcctctcagtaacagatagtattgaattcATAACTTCGTATAGCATACATTATACGAAGTTATccgaagggaag
gactgtcttactcaatgctctttgaattagtgaatgcatttatttactttgtgttgtaactgtgctcaaagcttcatctgccacgtttccctcacttgt
acatagttttcacagtgcttgaagagtcttactg

The injected zygotes were cultured overnight, the next day the embryos that developed to the 2-cell stage were transferred to the oviducts of pseudo pregnant CD1 female surrogates. Following optimization of the cycling conditions, the potential founder mice were genotype with the following primers pair, using Q5 High-Fidelity DNA Polymerase (NEW ENGLAND BIOLABS, Cat. no. M0491L). The body weight of male adult mice was measured weekly.

Rbbp5 genotyping forward primer: AGTTCAGAGCTGGTTTCCAAC

Rbbp5 genotyping reverse primer: AGGTAATGCCCATGTGAGCC

Biological rhythm study in mice

All mice used for biological rhythm study are in C57BL/6J background, male and between 3 and 4 months of age. Wild-type C57BL/6J mice (n=12), *Rbbp5* (flox/flox); Alb-CRE (-/-) (n=48) and *Rbbp5* (flox/flox); Alb-CRE (+/-) mice (n=48) [*Rbbp5* (flox/flox); Alb-CRE (-/-) and *Rbbp5* (flox/flox); Alb-CRE (+/-) mice were littermates] were first entrained under LD12:12 conditions for 2 weeks before transferred to constant darkness for 24hrs. Mice were then sacrificed via cervical dislocation at a 2h interval [for *Rbbp5* (flox/flox); Alb-CRE (-/-) and *Rbbp5* (flox/flox); Alb-CRE (+/-) mice] or 4h interval (for wild-type C57BL/6J mice) for a total of 48 hours under constant darkness. Mice were fed *ad libitum* during the entire experiment. The animal studies were carried out in accordance with the National Institutes of Health guidelines and were granted formal approval by the University of Pittsburgh's Institutional Animal Care and Use Committee (approval number IS00013119 and IS00013119).

Food intake and locomotor activity monitoring

Promethion Multi-plexed Metabolic Cage System was used for real-time measuring of food intake and locomotor activity. Male *Rbbp5* ^{Flox} and *Rbbp5* ^{LKO} mice between 3 and 4 months of age were acclimated to the chambers and ad libitum food intake was monitored for 48 hours under LD12:12 followed by 48 hours of constant darkness. n=6 for *Rbbp5* ^{Flox} and n=8 for *Rbbp5* ^{LKO} mice for LD12:12 study. n=5 for *Rbbp5* ^{Flox} and n=3 for *Rbbp5* ^{LKO} mice for DD study.

ER stress induction study in mice

For acute ER stress induction experiment, male littermates *Rbbp5* (flox/flox); Alb-CRE (-/-) and *Rbbp5* (flox/flox); Alb-CRE (+/-) mice between 5 and 7 months of age were randomly divided into two groups, and intraperitoneally injected with 0.05mg/kg body weight of tunicamycin dissolved in 500ul 3% DMSO in PBS or vehicle control (3% DMSO in PBS), respectively. Mice were injected with Tu between 9~10am in the morning and 8 hours later dissected for transcriptomic and western blot analysis for different tissues. The sample size is n=3 for *Rbbp5* ^{Flox} DMSO, n=3 for *Rbbp5* ^{Flox} Tu, n=4 for *Rbbp5* ^{LKO} DMSO, n=4 for *Rbbp5* ^{LKO} Tu.

For experiments involving RBBP5 liver-overexpressing mice, AAV8-TBG-EGFP and AAV8-TGB-mRBBP5 viruses were customarily designed and produced from Vector Biolab (Malvern, PA). Male wildtype C57BL/6J mice between 2 and 3 months of age were tail-vein injected with 0.5x10^11 genome copies of AAV8-TBG-EGFP or AAV8-TGB-mRBBP5 virus diluted in 100 µl of PBS. 30 days later, mice injected with either viruses were randomly divided into two cohorts and intraperitoneally injected with 0.05mg/kg body weight of tunicamycin dissolved in 500ul 3% DMSO in PBS or vehicle control (3% DMSO in PBS). Mice were injected with Tu between 9~10am in the morning and 8 hours later dissected for transcriptomic and western blot analysis for different tissues. The sample size is n=3 for AAV8-TBG-EGFP DMSO, n=4 for AAV8-TBG-EGFP Tu, n=4 for AAV8-TGB-mRBBP5 DMSO and n=4 for AAV8-TGB-mRBBP5 Tu.

For chronic ER stress induction experiment, male littermates *Rbbp5* (flox/flox); Alb-CRE (-/-) and *Rbbp5* (flox/flox); Alb-CRE (+/-) mice between 5 and 7 months of age were intraperitoneally injected with 0.025mg/kg body weight of tunicamycin dissolved in 500ul 3% DMSO in PBS or vehicle control (3% DMSO in PBS) daily for six consecutive days. Mice were injected with Tu between 9~10am in the morning and 24 hours after the last injection dissected for transcriptomic, western blot analysis, histology for liver tissues. The sample size is n=4 for *Rbbp5* ^{Flox} DMSO, n=4 for *Rbbp5* ^{Flox} Tu, n=2 for *Rbbp5* ^{LKO} DMSO, n=3 for *Rbbp5* ^{LKO} Tu.

Oil Red O Staining

Frozen sections were rinsed with PBS and then fixed with 10% neutral buffered formalin for 30 min at RT. After washing twice with deionized water, 60% isopropanol was applied to the fixed cells for 5 min, followed by a freshly prepared working solution of 1.5 mg/ml Oil Red O in isopropanol for 5 min at RT. The stained, fixed tissues were then rinsed with tap water until clear, covered with tap water and viewed on a phase contrast microscope. Size and areas of lipid droplet were quantified by customarily written pipelines in CellProfiler (v4.1.3).

Generation of stable autophagy reporter and ER-phagy reporter cell line

Primary MEFs were isolated from *Rbbp5* (flox/flox); Rosa26 CRE (+/+) mice and immortalized with SV40 lentivirus as previously described (32). For mCherry-EGFP-LC3B-expressing autophagy reporter MEFs, lentiviruses packaged in HEK293T cells with co-transfection of pCDH-EF1a-mCherry-EGFP-LC3B, pMD2.G and psPAX2 plasmids were used to infect *Rbbp5* (flox/flox); Rosa26 CRE (+/+) MEFs with a multiplicity of infection (MOI) of 3 for three times to achieve near complete infection. For mCherry-RAMP4-expressing ER-phagy reporter MEFs, lentiviruses packaged in HEK293T cells with co-transfection of pLenti-X1-hygro-mCherry-RAMP4, pMD2.G and psPAX2 plasmids were used to infect *Rbbp5* (flox/flox); Rosa26 CRE (+/+) MEFs with a multiplicity of infection (MOI) of 3. Stable MEFs were selected in the presence of 200µg/ml hygromycin.

siRNA Transient Transfections

Immortalized MEFs isolated from wild-type C57BL/6J mice were transfected with 10µM of different siRNAs for 24~48 hours with Lipofectamine RNAiMAX reagents (Life technologies) per the manufacturer's instructions. Source of siRNA are as follows: siGENOME non-targeting siRNA

214 pool (Dharmacon, D-001206-1305), siGENOME SMARTpool mouse *Rbbp5* siRNA (Dharmacon,
215 L-054560-01-0005), siGENOME SMARTpool mouse *Ash2l* siRNA (Dharmacon, L-048754-01-
216 0005), siGENOME SMARTpool mouse *Setd1a* siRNA (Dharmacon, L-051358-01-0005),
217 siGENOME SMARTpool mouse *Kat2a/Gcn5* siRNA (Dharmacon, L-040665-01-0005),
218 siGENOME SMARTpool mouse *Kat2b/Pcaf* siRNA (Dharmacon, L-049885-01-0005) and
219 siGENOME SMARTpool mouse *Xbp1* siRNA (Dharmacon, L-040825-00-0005). MEFs were
220 transfected with 10μM of different siRNAs for 48 hours and treated with DMSO or 100ng/ml of
221 tunicamycin for 8h.

222 **Real-time Luminescence Assay**

223 Stable *Manf*-dluc MEFs were transfected with non-targeting, *Rbbp5,* or *Ash2l* siRNA for 48 hours
224 in DMEM (4.5g/L glucose) supplemented with 10% FBS and treated with 25ng/ml tunicamycin in
225 DMEM for 2h before subjected to real-time luminescence assay using a Lumicycle (Actimetrics)
226 as previously described (33). Briefly, after tunicamycin treatment, MEFs were washed with 1x
227 PBS and cultured with DMEM (4.5g/L glucose) supplemented with 0.1 mM luciferin and 10mM
228 HEPES buffer in 35 mm tissue culture dishes in the absence of serum and transferred immediately
229 to Lumicycle for real-time luminescence analysis. Periods of oscillation were identified by
230 embedded Periodogram function.

231 **Immunofluorescence (IF)**

232 Immunofluorescence was performed as previously described (17). Briefly, liver OCT sections
233 were fixed in cold acetone for 10 mins at -20 ºC. The sections were then air dried, rehydrated with
234 PBS and permeabilized with PBS+ 0.1% Triton X-100. The sections were then blocked with 10%
235 goat serum at room temperature for 1 hour. Primary antibody against RBBP5 (Bethyl, A300-109A)
236 was added to the OCT section at 1:1000 dilution overnight at 4 ºC. Next day, sections were
237 washed three times with PBS and stained with Alexa-555 anti-rabbit secondary antibody at room
238 temperature for 2 hours. After that, the sections were washed with PBS three times and
239 counterstained with DAPI before mounting (with ProlongGold Glass) and imaging using Leica
240 SP8 lightening confocal microscope (Leica Microsystems).

241 **Time-lapse microscopy for autophagy reporter MEFs**

242 Time-lapse imaging was performed using SP8 lightening confocal microscope (Leica
243 Microsystems) with Okolab stage top incubator to maintain constant CO_2 (5%), temperature (37
244 ºC) and humidity (90%). mCherry-EGFP-LC3B-expressing *Rbbp5* (flox/flox); Rosa26 CRE (+/+)
245 MEFs were plated into 8-well chamber slides in full DMEM media and treated with (to deplete
246 RBBP5) or without tamoxifen (3μM/ml) for seven days before replacing with full DMEM or leucine-
247 free media counterstained with DAPI and images were taken every 2 hours for a total of 16 hours.
248 The number of cytosolic autophagosomes (GFP and mCherry double positive foci) and
249 autolysosomes (GFP negative and mCherry positive foci) per cell were quantified manually.

250 **Immunoblot**

251 Nuclear extracts were made from liver according to previously published protocol (34). Whole cell
252 lysates were lysed in RIPA buffer as previously described (17). Protein concentrations were
253 determined by Bradford assays (Bio-Rad), and aliquots were snap-frozen in liquid nitrogen and
254 stored at -80°C until usage. Immunoblot analyses were performed as described previously (35).
255 Briefly, 25~50μg proteins separated by 4~20% gradient SDS-PAGE gels (Biorad) were transferred
256 to nitrocellulose membranes, blocked in TBST buffer supplemented with 5% bovine serum
257 albumin (BSA) or 5% fat-free milk and incubated overnight with primary antibody anti-PERK (Cell
258 signaling, #3192), anti-phospho-PERK (Thr908) (Thermo Fisher, MA5-15033), anti-ATF4 (Cell
259 signaling, #11815), anti-IRE1α (Cell signaling, #3294), anti-phospho-IRE1α (Ser724) (ABclonal,

AP0878), anti-XBP1s (Biolegend, 658802), anti-RBBP5 (Bethyl, A300-109A), anti-RBBP5 (D3I6P) (Cell signaling, #13171), anti-WDR5 (Cell signaling, #13105), anti-ASH2L (Bethyl, A300-489A), anti-ASH2L (Bethyl, A300-112A), anti-SETD1A (Diagenode, CS-117-100), anti-SETD1B (Diagenode, CS-118-100), anti-MLL1-c (D6G8N) (Cell signaling, #14197), anti-mCherry (E5D8F) (Cell signaling, #43590), anti-p62/SQSTM1 (Santa Cruz, sc-28359) and anti-β-ACTIN (Cell signaling, #12620) at 4°C. Blots were incubated with an appropriate secondary antibody coupled to horseradish peroxidase at room temperature for 1 hour, and reacted with ECL reagents per the manufacturer's (Thermo) suggestion and detected by Biorad ChemiDoc MP Imaging System.

Co-Immunoprecipitation (Co-IP)

Nuclear extracts (NE) were made from liver according to our published protocol (34). Protein concentrations were determined by Bradford assays (Bio-Rad), and aliquots were snap-frozen in liquid nitrogen and stored at -80°C until usage. 200 µg of NE was used for per IP. 5 µg of different antibodies or control IgG were coupled to 1.5 mg of magnetic Dynabeads (Life Technologies) for every IP using Dynabeads Antibody Coupling Kit (Life Technologies) per manufactures' protocol. Co-IP was essentially carried out as previously described (36) except that coupled antibody Dynabeads was added to the NEs for incubation. The antibodies used for Co-IP are as follows: anti-XBP1s (Biolegend, 658802).

qRT-PCR

Total mRNA was isolated from murine embryonic fibroblasts (MEFs) or mouse liver with PureLink RNA mini kit (Life Technologies) with additional on-column DNase digestion step to remove genomic DNA per the manufacturer's instructions. Reverse transcription was carried out using 5µg of RNA using Superscript III (Life Technologies) per the manufacturer's instructions. For gene expression analyses, cDNA samples were diluted 1/30-fold (for all other genes except for 18sRNA) and 1/900-fold (for 18sRNA). qPCR was performed using the SYBR green system with sequence-specific primers. All data were analyzed with 18S or *β-actin* as the endogenous control. qPCR primer sequences are as follows and all primers span introns, except for primers for quantifying pre-mRNAs:
Mouse *Rbbp5* forward primer: CAGAGCCTATGCAGAAGCTGCA
Mouse *Rbbp5* reverse primer: CTTCACCAGGTTGCCAATGCTC
Mouse *Ddit3* forward primer: GGAGGTCCTGTCCTCAGATGAA
Mouse *Ddit3* reverse primer: GCTCCTCTGTCAGCCAAGCTAG
Mouse *Creld2* forward primer: CTACACCAAGGAGAGTGGACAG
Mouse *Creld2* reverse primer: TCTGTCTCCTCAAAGCCTTCCG
Mouse *Hspa5* forward primer: TGTCTTCTCAGCATCAAGCAAGG
Mouse *Hspa5* reverse primer: CCAACACTTCCTGGACAGGCTT
Mouse *Dnajb11* forward primer: TGTGACCGTCTCACTGGTTGAG
Mouse *Dnajb11* reverse primer: CCCTTTCTTCCACAGCTTGGCT
Mouse *Pdia4* forward primer: TGGGCTCTTTCAGGGAGATGGT
Mouse *Pdia4* reverse primer: GGGAGACTTTCAGGAACTTGGC
Mouse *Hsp90b1* forward primer: GTTTCCCGTGAGACTCTTCAGC
Mouse *Hsp90b1* reverse primer: ATTCGTGCCGAACTCCTTCCAG
Mouse *Syvn1* forward primer: CCAACATCTCCTGGCTCTTCCA
Mouse *Syvn1* reverse primer: CAGGATGCTGTGATAAGCGTGG
Mouse *Gdf15* forward primer: ACTCAGTCCAGAGGTGAGATTG
Mouse *Gdf15* reverse primer: GGGGCCTAGTGATGTCCCAG
Mouse *Il1a* forward primer: ACGGCTGAGTTTCAGTGAGACC
Mouse *Il1a* reverse primer: CACTCTGGTAGGTGTAAGGTGC
Mouse *Il1b* forward primer: TGGACCTTCCAGGATGAGGACA

308 Mouse *Il1b* reverse primer: GTTCATCTCGGAGCCTGTAGTG
309 Mouse *Fga* forward primer: GGATTCTAACTCACTGACCAGGA
310 Mouse *Fga* reverse primer: CCTCAGGATCTCAATTCTGCGC
311 Mouse *C3* forward primer: CGCAACGAACAGGTGGAGATCA
312 Mouse *C3* reverse primer: CTGGAAGTAGCGATTCTTGGCG
313 Mouse *Tifa* forward primer: AGCAAGAAAACCAGTTTGATGGTAG
314 Mouse *Tifa* reverse primer: GCAACAGGAACTGATACTCTCCG
315 Mouse *Fgl1* forward primer: GGAAACTGTGCTGAGGAAGAGC
316 Mouse *Fgl1* reverse primer: TCCGTTTCTGCCCTGTAGGAAC
317 Mouse *Fgb* forward primer: TGACACCTCCATCAAGCCGTAC
318 Mouse *Fgb* reverse primer: GGTCCCATTTCCTGCCAAAGTC
319 Mouse *Il6* forward primer: CTTCCATCCAGTTGCCTTCT
320 Mouse *Il6* reverse primer: CTCCGACTTGTGAAGTGGTATAG
321 Mouse *Herpud1* forward primer: acctgagccgagtctaccc
322 Mouse *Herpud1* reverse primer: aacagcagcttcccagaataaa
323 Mouse *Nbr1* forward primer: GGATTTAAAGCACCTCCTGATTCC
324 Mouse *Nbr1* reverse primer: ATTGGGTCCCACTCAGGTCT
325 Mouse *Sesn2* forward primer: CTGGCCGAACTCATCCAAG
326 Mouse *Sesn2* reverse primer: CTGCCTCATGCGTTCCATC
327 Mouse *Sqstm1* forward primer: AACAGATGGAGTCGGGAAAC
328 Mouse *Sqstm1* reverse primer: AGACTGGAGTTCACCTGTAGA
329 Mouse *Stbd1* forward primer: CTGGGAAGTAGATGGGAAAGTG
330 Mouse *Stbd1* reverse primer: TCGGTGTTTGTGGTGTAGTG
331 Mouse *Sirt1* forward primer: TGACAGAACGTCACACGCCA
332 Mouse *Sirt1* reverse primer: ATTGTTCGAGGATCGGTGCCA
333 Mouse *Gcn5* forward primer: TTGATTGAGCGCAAACAGGC
334 Mouse *Gcn5* reverse primer: CAGCCTGTCTCTCGAATGCC
335 Mouse *Pcaf* forward primer: CGTGAAGAAGGCGCAGTTG
336 Mouse *Pcaf* reverse primer: CAGGACTCCTCTGCCTTGC
337 Mouse *Ash2l* forward primer: gctgtgtctgctagtgggaac
338 Mouse *Ash2l* reverse primer: catcttgctgcttacgcttg
339 Mouse *Setd1a* forward primer: gggtagcacccctactctc
340 Mouse *Setd1a* reverse primer: gggtttgaaggaggttgaagt
341 Mouse *Eif2ak3* forward primer: ccttggtttcatctagcctca
342 Mouse *Eif3ak3* reverse primer: atccagggaggggatgat
343 Mouse total *Xbp1* forward primer: gggtctgctgagtcc
344 Mouse total *Xbp1* reverse primer: cagactcagaatctgaagagg
345 Mouse *Sec23b* forward primer: tgaccaaactggacttctgga
346 Mouse *Sec23b* reverse primer: aaagaatctcccatcaccatgt
347 Mouse *Manf* forward primer: gacagccagatctgtgaactaaaa
348 Mouse *Manf* reverse primer: tttcacccggagcttcttc
349 Mouse *Hyou1* forward primer: GAGGCGAAACCCATTTTAGA
350 Mouse *Hyou1* reverse primer: GCTCTTCCTGTTCAGGTCCA
351 Mouse *Atf4* forward primer: CCACTCCAGAGCATTCCTTTAG
352 Mouse *Atf4* reverse primer: CTCCTTTACACATGGAGGGATTAG
353 Mouse *Atf6* forward primer: CATGAAGTGGAAAGGACCAAATC
354 Mouse *Atf6* reverse primer: CAGCCATCAGCTGAGAATTAGA
355 Mouse 18s RNA forward primer: ctcaacacgggaaacctcac
356 Mouse 18s RNA reverse primer: cgctccaccaactaagaacg
357 Mouse *β-actin* forward primer: aaggccaaccgtgaaaagat
358 Mouse *β-actin* reverse primer: gtggtacgaccagaggcatac

359 **RNA-Seq to identify RBBP5-dependent 12h hepatic transcriptome**

360 Mouse liver tissues were collected from *Rbbp5* ^{Flox} (n=2) and *Rbbp5* ^{LKO} (n=2) mice at 2h intervals
361 for a total of 48 hours under constant darkness condition. Total RNA was isolated from mouse
362 liver with miRNeasy Mini Kit (Qiagen) per the manufacturer's instructions. RNA was assessed for
363 quality using an Agilent TapeStation 4150/Fragment Analyzer 5300 and RNA concentration was
364 quantified on a Qubit FLEX fluorometer. Libraries were generated with the Illumina Stranded
365 mRNA Library Prep kit (Illumina: 20040534) according to the manufacturer's instructions. Briefly,
366 200 ng of input RNA was used for each sample. Following adapter ligation, 12 cycles of indexing
367 PCR were completed, using IDT for Illumina RNA UD Indexes (Illumina: 20040553-6). Library
368 quantification and assessment was done using a Qubit FLEX fluorometer and an Agilent
369 TapeStation 4150/Fragment Analyzer 5300. The prepared libraries were pooled and sequenced
370 using NoveSeq 6000 (Illumina), generating an average of 40 million 2×100 bp paired end reads
371 per sample. RNA-Seq library preparation and sequencing were performed at UPMC Genome
372 Center. Raw RNA-seq FASTQ files were analyzed by FastQC for quality control. Adaptors and
373 low-quality reads were filtered by Trimmomatic (37). Then the processed reads were aligned by
374 HISAT2 (38) against mouse reference mm10. Gene and isoform FKPM values were calculated
375 by Cufflinks. Since the background gene expression level is FPKM=0.1 in mouse liver (21), only
376 those genes with average gene expression across 48 hours in Rbbp5 ^{Flox} mice larger than 0.1
377 were included for rhythm-identification analysis. Averaged FPKM values at each time were used
378 for cycling transcripts identification by the eigenvalue/pencil method. Raw temporal data was
379 subject to polynomial detrend (n=2) first, and superimposed oscillations were identified using
380 previously described eigenvalue/pencil method on the detrended dataset (23,39). Specifically,
381 three oscillations were identified from each gene. Criterion for circadian gene is period between
382 21h to 27h, decay rate between 0.9 and 1.1; for ~12hr genes: period between 10h to 13h, decay
383 rate between 0.9 and 1.1. The relative amplitude is calculated via dividing the amplitude by the
384 mean expression value of each gene. All analysis were performed in MatlabR2017A. Heat maps
385 were generated by Gene Cluster 3.0 and TreeView 3.0 alpha 3.0 using log2 mean-normalized
386 values. RAIN analysis was performed as previously described in Bioconductor (3.4)
387 (http://www.bioconductor.org/packages/release/bioc/html/rain.html) (40) using the full detrended
388 dataset with duplicated at each time point.

389 For the eigenvalue method, every gene consists of multiple superimposed oscillations.
390 Therefore, we define a circadian gene as any gene that exhibits a superimposed circadian rhythm,
391 regardless of its relative amplitude compared to other superimposed oscillations. Similar
392 definitions apply to 12hr genes. Under this definition, a gene can be both a circadian and 12hr-
393 cycling gene. By comparison, we define a dominant circadian gene as any gene whose
394 superimposed circadian rhythm has the largest amplitude among all oscillations. Similar
395 definitions also apply to 12hr genes. Under this definition, dominant circadian and dominant 12hr
396 genes are mutually exclusive.

397 **RNA-seq for identifying RBBP5-dependent acute transcriptional response to ER stress**

398 Mouse liver tissues were collected from *Rbbp5* ^{Flox} and *Rbbp5* ^{LKO} mice intraperitoneally treated
399 with or without Tu for 8 hours. Total mRNA was isolated from mouse liver with PureLink RNA mini
400 kit (Life Technologies) with additional on-column DNase digestion step to remove genomic DNA
401 per the manufacturer's instructions. Detailed procedures for transcriptome sequencing were
402 described previously(41) and were supported by the Genomics and Systems Biology Core of the
403 Pittsburgh Liver Research Center. Briefly, the mRNA samples per mouse were processed into
404 short-read libraries using the Bio-Rad SEQuoia Dual Indexed Primers. Next, the circularization
405 was performed using the Element Biosciences Adept Library Compatibility Kit v1.1 based on the
406 manufacturer's instructions, followed by the quantification using qPCR with the provided standard.

407 Finally, the libraries were measured by the Element Biosciences AVITI system to sequence paired
408 end reads with 75 bp each. The raw FASTQ files from RNA-seq were trimmed by Trimmomatic
409 (42) to filter out low-quality reads. The surviving reads were then aligned to the mouse mm10
410 reference genome by STAR aligner(43). Fragments Per Kilobase of transcript per Million mapped
411 reads (FPKM) values per library were quantified by the tool Cufflinks(44). Log 2 normalized fold
412 induction and adjusted p values between *Rbbp5* ^{Flox} DMSO and *Rbbp5* ^{LKO} DMSO, *Rbbp5* ^{Flox} Tu
413 and *Rbbp5* ^{LKO} Tu, *Rbbp5* ^{Flox} DMSO and *Rbbp5* ^{Flox} Tu, and *Rbbp5* ^{LKO} DMSO and *Rbbp5* ^{LKO} Tu
414 were calculated by using the iDEP (integrated Differential Expression and Pathway analysis)
415 online application (45).

416 **Chromatin Immunoprecipitation (ChIP)-Seq and ChIP-qPCR**

417 ChIP for RBBP5 was performed using anti-RBBP5 antibody (Bethyl, A300-109A) as previously
418 described (21). Briefly, mouse liver samples were submerged in PBS + 1% formaldehyde, cut into
419 small (~1 mm3) pieces with a razor blade and incubated at room temperature for 15 minutes.
420 Fixation was stopped by the addition of 0.125 M glycine (final concentration). The tissue pieces
421 were then treated with a TissueTearer and finally spun down and washed twice in PBS. Chromatin
422 was isolated by the addition of lysis buffer, followed by disruption with a Dounce homogenizer.
423 The chromatin was enzymatically digested with MNase. Genomic DNA (Input) was prepared by
424 treating aliquots of chromatin with RNase, Proteinase K and heated for reverse-crosslinking,
425 followed by ethanol precipitation. Pellets were resuspended and the resulting DNA was quantified
426 on a NanoDrop spectrophotometer. An aliquot of chromatin (30 µg) was precleared with protein A
427 agarose beads (Invitrogen). Genomic DNA regions of interest were isolated using 4 µg of antibody.
428 Complexes were washed, eluted from the beads with SDS buffer, and subjected to RNase and
429 proteinase K treatment. Crosslinking was reversed by incubation overnight at 65 °C, and ChIP
430 DNA was purified by phenol-chloroform extraction and ethanol precipitation. The DNA libraries
431 were prepared at the University of Pittsburgh and sequenced at Gene by Gene, Ltd per standard
432 protocols. DNA libraries were prepared with Ovation® Ultralow V2 DNA-Seq library preparation
433 kit (NuGen) using 1ng input DNA. The size selection for libraries was performed using SPRIselect
434 beads (Beckman Coulter) and purity of the libraries were analyzed using the High Sensitivity DNA
435 chip on Bioanalyzer 2100 (Agilent). The prepared libraries pooled and sequenced using Nova-
436 Seq 6000 (Illumina), generating ~30 million 75 bp single-end reads per sample. ChIP-qPCR for
437 MEFs were essentially performed the same way as previously described with anti-RBBP5 (Bethyl,
438 A300-109A) and anti-H3K4me3 (Active Motif, 61379) antibodies, except that the MEFs were
439 directly fixed with 1% formaldehyde before subject to nuclei isolation and chromatin
440 immunoprecipitation. The primers used for ChIP-qPCR are as follows:
441 Negative control region 1 forward primer: GCAACAACAACAGCAACAATAAC
442 Negative control region 1 reverse primer: CATGGCACCTAGAGTTGGATAA
443 *Manf* promoter forward primer: CCCTTAAATGGGTCAACGTCTC
444 *Manf* promoter reverse primer: GGCGCTAAACCCAAGGAAA
445 *Xbp1* promoter forward primer: TCCGTACGGTGGGTTAGAT
446 *Xbp1* promoter reverse primer: ACCTTCTTCTGTGCCTGTG
447 *Hyou1* promoter forward primer: CCGTGTGGGTACGTCCT
448 *Hyou1* promoter reverse primer: GACGGCTGCTCCATCCT
449 *Sesn2* promoter forward primer: ACAGGAGGCCGGGACTA
450 *Sesn2* promoter reverse primer: CTGGGCTGAAAGGAGTGTCTAT

451 **ChIP-Seq analysis**

452 The sequences identified were mapped to the mouse genome (UCSC mm10) using BOWTIE
453 function in Galaxy Deeptool (https://usegalaxy.org/) (46). Only the sequences uniquely mapped
454 with no more than 2 mismatches were kept and used as valid reads. PCR duplicates were also

455 removed. Peak calling was carried out by MACS2 (version 2.1.1.20160309) in Galaxy (options --
456 mfold 5, 50 --pvalue 1e-4), on each ChIP-seq file against input. To account for the different
457 sequencing depths between samples, the BAM files generated from MACS2 were RPKM
458 normalized to sequencing depth using the bamCoverage function in Galaxy Deeptool and the
459 bigwig files were generated accordingly. The relative intensity of each RBBP5 binding site is
460 further calculated via the computeMatrix function with the RPKM normalized bigwig files and bed
461 files from the peak calling as inputs by calculating the area under the curve.

462 **Proximity labeling**

463 Proximity labeling was performed using Protein A-TurboID as previously described (47). Briefly,
464 target cells were grown to 90-100% confluency in 15 cm dishes, harvested in PBS using a cell
465 scraper, and pelleted by centrifugation. Nuclei was isolated by resuspending the cell pellet in ice-
466 cold HLB buffer, incubating on ice, and washing through sequential centrifugation steps. Isolated
467 nuclei were incubated with digitonin buffer containing ~2 µg of IgG or H3K4me3 antibody (Active
468 Motif, 61379) for 20 minutes at room temperature with shaking, followed by incubation with 1.4
469 µg of Protein A-TurboID for 30 minutes at 4°C. After washing, biotinylation was induced by
470 incubating samples in biotinylation buffer (containing ATP, $MgCl_2$, and 500 µM biotin) for 10
471 minutes at 37°C. Nuclei were lysed in RIPA buffer at 4°C overnight, sonicated, and centrifuged to
472 collect the supernatant. Streptavidin affinity purification was performed by incubating lysates with
473 M-270 streptavidin beads for 2 hours at room temperature or overnight at 4°C. Beads were
474 washed extensively with RIPA buffer, and bound proteins were eluted by boiling at 100°C for 15
475 minutes in 70 µL of 1.5X LDS buffer. Samples were clarified by centrifugation and magnetic
476 separation.

477 For protein identification, half of each sample was separated ~1.5 cm on a 10% Bis-Tris Novex
478 mini-gel (Invitrogen) using the MES buffer system. The gel was stained with Coomassie, and each
479 lane was excised into ten equally sized segments. Gel pieces were processed using a DigestPro
480 robot (CEM) with the following protocol: washes with 25 mM ammonium bicarbonate and
481 acetonitrile, reduction with 10 mM dithiothreitol at 60°C, alkylation with 50 mM iodoacetamide at
482 room temperature, digestion with trypsin (Promega) at 37°C for 4 hours, and quenching with
483 formic acid. The resulting peptides were analyzed by nano LC-MS/MS using a Waters M-class
484 HPLC system interfaced with a ThermoFisher Fusion Lumos mass spectrometer. Peptides were
485 loaded onto a trapping column and eluted over a 75 µm analytical column at 350 nL/min with a
486 30-minute gradient. MS and MS/MS spectra were acquired in the Orbitrap at resolutions of 60,000
487 and 15,000 FWHM, respectively. Data was searched using Mascot against the SwissProt Mouse
488 database with a 10 ppm peptide mass tolerance and a 20 ppm fragment mass tolerance. Search
489 parameters included trypsin digestion, fixed carbamidomethylation of cysteines, and variable
490 modifications such as oxidation (M), acetylation (protein N-term), deamidation (NQ), and pyro-glu
491 (N-term Q). Data was processed using Scaffold software with a 1% false discovery rate (FDR) at
492 both the protein and peptide levels, requiring at least two unique peptides per protein.

493 **Gene ontology analysis**

494 DAVID (Version 2021) (48) (https://david.ncifcrf.gov) was used to perform Gene Ontology
495 analyses. Briefly, gene names were first converted to DAVID-recognizable IDs using Gene
496 Accession Conversion Tool. The updated gene list was then subject to GO analysis using all
497 Homo Sapiens as background and with Functional Annotation Chart function. GO_BP_DIRECT,
498 KEGG_PATHWAY or UP_KW_BIOLOGICAL_PROCESS was used as GO categories. Only GO
499 terms with a p value less than 0.05 were included for further analysis.

500 **Motif analysis**

501 Motif analysis was performed with the SeqPos motif tool (version 0.590) (49) embedded in Galaxy
502 Cistrome using all motifs within the mouse reference genome mm10 as background. LISA
503 analysis was performed using webtool (http://lisa.cistrome.org/).

504 **Statistical Analysis**

505 Data were analyzed and presented with GraphPad Prism software. Plots show individual data
506 points and bars at the mean and ± the standard error of the mean (SEM). One-tailed t-tests were
507 used to compare means between groups, with significance set at $p < 0.05$. In instances where
508 the p value is not shown, *, **, ***, and **** represent $p < 0.05$, 0.01, 0.001, and 0.0001,
509 respectively.

510 **Results:**

511 **Global RBBP5 binding to chromatin exhibits a ~12h ultradian rhythm, concomitant with**
512 **the promoter-proximal ~12h H3K4me3, but not H3K9Ac/H3K27Ac rhythms in mouse liver.**

513 The 12h oscillator is transcriptionally regulated by the UPR TF XBP1s in mice (18,19,21), and
514 likely under control by additional bZIP TFs, such as ATF4 and ATF6 (50). However, decades of
515 research of eukaryotic gene regulation demonstrated that TFs themselves are not sufficient to
516 drive transcription initiation and elongation, and additional so-called "co-regulators" are required
517 for full gene activation by shaping the epigenetic landscape (51-53). Currently, the epigenetic
518 landscape of both the 12h oscillator and proteotoxic stress responses are poorly characterized.
519 To identify epigenetic regulators of global proteostasis control, we first examined a published
520 temporal hepatic epigenome dataset for histone modifications associated with the active
521 promoters of ~12h genes (54). We found ~12h rhythms of histone H3 trimethylated at lysine 4
522 (H3K4me3), but not two histone acetylation markers, histone H3 acetylated at lysine 9 (H3K9Ac)
523 and lysine 27 (H3K27Ac), at the promoters of ~12h genes (**Fig. 1A, B**). This is particularly
524 prominent for those ~12h genes with rhythmic expressions peaking at ZT0 and ZT12 that are
525 enriched for proteostasis pathways (21), with H3K4me3 level also peaking at these two time
526 points (**Fig. 1A, B**).

527 In eukaryotes, H3K4 is tri-methylated by the COMPASS complex, which includes regulatory
528 subunits RBBP5, ASH2L, WDR5, DPY30 and catalytic subunits SETD1A/B/MLL1-4 (**Fig. S1A**)
529 (55-57). Via writing H3K4me3, COMPASS is essential for the eviction of paused RNA polymerase
530 II (RNAPII) and promotes transcriptional elongation (58,59). Landscape In Silico deletion Analysis
531 (LISA) (60) further inferred COMPASS subunits WDR5, ASH2L, DYP30 and RBBP5 as putative
532 epigenetic regulators of hepatic ~12h, but not circadian genes (**Fig. S1B**). Being the commonly
533 shared regulatory subunits for all MLL family H3K4 methyl transferase complex (including
534 SETD1A/B and MLL1-4), RBBP5/ASH2L forms the minimal heterodimer sufficient to activate all
535 MLL histone methyl transferase **(61,62)** and are essential for the assembly of the whole
536 COMPASS complex **(57,63)**. Between the two essential subunits, we initially focused on RBBP5.
537 Eigenvalue/pencil method (64) revealed that the levels of both hepatic *Rbbp5* mRNA and nuclear
538 RBBP5 protein exhibit ~12h oscillations, with the nuclear protein level peaking at ~CT0 and
539 ~CT12 (**Fig. S1C, D**), in line with the acrophases of H3K4me3 and gene expression oscillations
540 (**Fig. 1A, B**).

541 To further evaluate the potential role of RBBP5 in establishing the epigenetic landscape of
542 hepatic ~12h rhythms, we performed temporal RBBP5 ChIP-seq at a 4-h interval for a total of 48
543 hours in the liver of male C57BL/6 mice housed under constant darkness condition fed *ad libitum*.
544 Chromatin occupancies of RBBP5 align well with nucleosome positioning downstream of the
545 transcription start sites (TSS) and the H3K4me3 epigenome, with 'ridges' corresponding to 130bp,
546 310bp, 490bp, 670bp downstream of TSS at all time points, thus demonstrating the high quality

547 of our ChIP-seq dataset (**Fig. 1C-F**). In total, we identified 7,963 hepatic RBBP5 binding sites that
548 are within 2kb (up and downstream) of TSS of 6,451 genes (**Fig. 1C and Table S1**). The average
549 binding intensities of RBBP5 on all post-TSS nucleosomes displayed robust 12h rhythms, with
550 peaks occurring at CT0, CT12, CT24, and CT36 (**Fig. 1C-E**). These rhythms aligned with the 12h
551 oscillations of promoter-proximal H3K4me3 (**Fig. 1C-E)**, but not with those of H3K9Ac or
552 H3K27Ac (**Fig. S1E**). This pattern is exemplified by *Xbp1*, one of the major UPR TFs and the
553 transcriptional regulator of the 12h oscillator, and *Hsph1*, a canonical 12h oscillator output gene
554 encoding a heat shock protein (**Fig. S1F**). Using the eigenvalue/pencil and RAIN (40) algorithms,
555 we identified 3,028 and 1,864 ($p<0.05$) RBBP5 binding sites that cycle with a ~12h period,
556 respectively (**Fig. S1G, H and Table S1**). Collectively, these results establish the epigenetic
557 landscape of hepatic 12h oscillator is marked by RBBP5-H3K4me3.

558 **Hepatic RBBP5 cistrome coincides with that of XBP1s and hepatic ~12h transcriptome.**

559 To investigate if RBBP5 regulates hepatic ~12h rhythms of gene expression, we first examined
560 the correlation between RBBP5 proximal promoter binding status and ~12h rhythms of gene
561 expression. As illustrated in **Fig. 2A**, genes with proximal promoter RBBP5 binding are enriched
562 for ~12h rhythms of gene expression (P=1.1e-39 by Chi-squared test). For those 2,525 ~12h
563 genes with RBBP5 binding, the phases of RBBP5 chromatin binding center around CT0 and CT12,
564 slightly preceding the phases of gene expression observed at ~CT1 and ~CT13 (**Fig. 2B**). This
565 temporal relationship suggests that RBBP5 acts as a driver, rather than a consequence of ~12h
566 rhythms of gene expression.

567 We next performed Gene Ontology (GO) analysis on those hepatic genes with proximal
568 promoter RBBP5 binding and revealed strong enrichment of proteostasis pathways including
569 protein processing in the ER and ubiquitin-mediated proteolysis (**Fig. 2C**). Additionally, pathways
570 involved in mRNA processing, such as spliceosome, RNA transport, and mRNA surveillance, were
571 also enriched (**Fig. 2C**). These findings align with previous observations that both mRNA and
572 protein metabolism pathways are enriched in genes exhibiting ~12h rhythms in both mice and
573 humans (16,17,65). The coupling of mRNA and protein metabolism is orchestrated by a SON-
574 XBP1s axis and involves the liquid-liquid phase separation (LLPS) dynamics of nuclear speckles
575 (17). Similar pathways are also enriched in genes exhibiting both ~12h rhythms of RBBP5
576 promoter binding and gene expression (**Fig. 2C**).

577 XBP1s is the major transcriptional factor regulating the hepatic 12h oscillator and also exhibits
578 a global 12h rhythm of chromatin binding to the promoter regions peaking at CT0, 12, 24 and 36
579 (19,21). Comparing the cistromes of RBBP5 and XBP1s revealed a significant overlap between
580 the two, with 920 genes sharing RBBP5 and XBP1s proximal promoter binding (**Fig. 2D**). Co-
581 immunoprecipitation in the hepatic nuclear extracts at CT0 confirmed the physical interaction
582 between XBP1s and subunits of SET1/COMPASS, including RBBP5, ASH2L, WDR5, and two
583 histone methyltransferase SETD1A and SETD1B (**Fig. 2E**). Motif analysis of the DNA sequences
584 around the 6,149 RBBP5 binding sites that do not overlap with XBP1s cistrome identified binding
585 motifs for GABPA, KLF, ATF6, NFYA and ATF4 (**Fig. 2F**). These findings suggest that, in addition
586 to acting as a co-activator for XBP1s, RBBP5 may also work with other transcription factors to
587 shape the hepatic 12h epigenome.

588 **RBBP5 is an epigenetic regulator of the ~12h oscillator, but not the canonical ~24h core**
589 **circadian clock.**

590 To establish the causality between RBBP5 and hepatic 12h rhythms of gene expression, we
591 generated RBBP5 liver hepatocyte-specific knockout (RBBP5 ^{LKO}) mice using the CRE-loxP
592 system. Exon 10 of mouse *Rbbp5,* which encodes the SET/ASH2L binding domain, was flanked
593 by loxP sites (**Fig. 3A**). CRE-mediated deletion of Exon 10 is expected to lead to a frameshift and

594 nonsense-mediated RNA decay of truncated *Rbbp5* transcript (**Fig. S2A**). Crossing homozygous
595 floxed *Rbbp5* mice with Albumin-CRE mice resulted in liver-specific deletion of RBBP5, which
596 was confirmed by DNA genotyping, IF against RBBP5 and western blot analysis (**Figs. 3B and**
597 **S2B-D**). The resulting RBBP5 ^{LKO} mice weighed slightly less than wild-type counterparts (**Fig.**
598 **S3A**) but maintained normal rhythmic locomotor activity and fasting-feeding cycles under both
599 12h:12h L/D and constant darkness conditions (**Fig. S3B-I**).

600 To identify the RBBP5-dependent oscillating hepatic transcriptome, we performed bulk RNA
601 sequencing (RNA-Seq) analysis in the liver of male *Rbbp5* ^{Flox} and *Rbbp5* ^{LKO} mice at 2-h intervals
602 for a total of 48 hour under constant darkness in duplicates (**Table S2**). To identify genes cycling
603 with a period ranging from 6 to 36 hours, we initially applied the RAIN algorithm (40) to each
604 genotype's temporal transcriptome (40) (**Table S3**). Compared to alternative methods like
605 JTK_CYCLE, RAIN detects rhythms with arbitrary waveforms and therefore more robustly
606 uncovers ultradian rhythms (21,23,39). Consistent with past studies (18,20,21,66,67), two
607 populations of hepatic transcripts cycling with periods of ~12h and ~24h were identified in *Rbbp5*
608 ^{Flox} mice liver (**Fig. 3C, D**). By contrast, in *Rbbp5* ^{LKO} mice, the ~12h rhythms are all but abolished
609 and the circadian oscillations remain largely intact, which include all core circadian clock genes
610 (such as *Bmal1*, *Per1/2/3*, and *Nr1d1/2*) displaying robust circadian rhythms with the same
611 phases and amplitudes as those observed in *Rbbp5* ^{Flox} mice (**Figs. 3C-F and S4A**). The
612 maintenance of ~24h circadian rhythms and abolishment of ~12h ultradian rhythms in *Rbbp5* ^{LKO}
613 mice is further confirmed by the principal component analysis (PCA) (**Fig. S4B, C**). Specifically,
614 using RAIN with an FDR cutoff of 0.01 and 0.05, we identified a total of 3,549 and 6,025 hepatic
615 transcripts cycling at periods between 10-12h in *Rbbp5* ^{Flox} mice, respectively. By contrast, only
616 61 and 813 10-12h genes were observed in *Rbbp5* ^{LKO} mice with the same FDR thresholds,
617 indicating over 93% ~12h hepatic transcriptome was abolished with liver RBBP5 ablation (**Figs.**
618 **3G, H, S4D and Table S3**). GO analysis confirmed that these RBBP5-depenent ~12h hepatic
619 transcriptomes are enriched in various mRNA processing and proteostasis pathways, distinct from
620 those of RBBP5-independent circadian genes enriched in lipid metabolism and phosphorylation
621 (**Fig. 3I**).

622 To determine the robustness of our results to different analytic methods, we also performed
623 spectrum analysis with the eigenvalue/pencil method (**Table S4**) (19-21,23,26,39), which unlike
624 statistical methods such as JTK_CYCLE and RAIN does not require pre-assignment of period
625 range, enabling unbiased identification of multiple superimposed oscillations for any given gene
626 (19-21,23,26,39). Revealing up to three oscillations from each gene, eigenvalue/pencil analyses
627 also revealed prevalent ~24h and ~12h oscillations in *Rbbp5* ^{Flox} mice, along with a third
628 population cycling at a period around 8h (**Fig. S5A-E**). Hepatic ~8h oscillations were also
629 previously reported but their regulation and function remained elusive (22,66). *Rbbp5* ^{LKO} mice,
630 on the other hand, exhibited a drastically different spectrum, characterized by the near complete
631 loss of the ~12h rhythms, *de novo* gains of many faster ultradian rhythms with periods between 6
632 and 7h, and the maintenance of most circadian rhythms (**Fig. S5A-E**). Similar findings were also
633 observed for dominant oscillations (which is the one with the largest amplitude among the three
634 superimposed oscillations for each gene) for each gene (**Fig. S5A-E**). For the ~12h genes
635 originally identified in *Rbbp5* ^{Flox} mice but lost in *Rbbp5* ^{LKO} mice, the period spectrum in the *Rbbp5*
636 ^{LKO} mice displayed a diverse distribution. This ranged from a complete lack of rhythmicity (~39%)
637 to shorter ultradian periods of 6-7 hours, and even to longer periods exceeding 24 hours (**Fig.**
638 **S5F**). RBBP5-dependent ~12h transcriptome uncovered by the eigenvalue/pencil showed
639 substantial overlap with the results obtained through the RAIN method. This convergence was
640 evident both in the specific genes identified (**Fig. S5C**) and in the enriched biological pathways
641 (**Fig. S5G, H**), thereby confirming the robustness of our findings. These results thus establish

642 RBBP5 as a central epigenetic regulator of the hepatic 12h oscillator, with more than 90% ~12h
643 hepatic transcriptome abolished in its absence.

644 In addition to liver, cell-autonomous ~12h rhythms of proteostasis gene expression including
645 *Xbp1* can also be observed in mouse embryonic fibroblasts (MEFs) synchronized by low
646 concentration of ER stress inducer tunicamycin (Tu) **(21,23)**. We observed a ~12h rhythm of
647 *Rbbp5* expression in Tu-synchronized MEFs, which is independent of BMAL1 but require XBP1s
648 (**Fig. S6A**), indicating RBBP5 itself is also under 12h oscillator control. To test the functional role
649 of COMPASS in regulating the cell-autonomous ~12h rhythms, we knocked down either *Rbbp5*
650 or *Ash2l* via siRNA in a previously described 12h oscillator reporter MEFs that stably express
651 *Manf* promoter-driven destabilized luciferase (dluc) (21), and found that both siRNAs significantly
652 dampen the ~12h oscillation of luciferase activity as well as shorten the period (**Fig. S6B**). By
653 contrast, neither *RBBP5* nor *ASH2L* knocking down affects the circadian oscillation of *Bmal1*
654 promoter activity in human U2OS cells in a previous genome-wide siRNA screen study (68) (**Fig.**
655 **S6C**). Collectively, our results demonstrate that RBBP5 is an integral component of the 12h
656 oscillator, but dispensable for the canonical circadian clock both *in vivo* and *in vitro*.

657 **RBBP5 modulates the hepatic transcriptional response to acute proteotoxic stress *in vivo*.**

658 Before the discovery of the mammalian 12h oscillator, the dynamics of proteostasis were primarily
659 studied as transient responses to various proteotoxic stresses, with a classic example being the
660 UPR triggered by ER stress. In response to the accumulation of misfolded proteins in the ER, the
661 UPR initiates a signaling cascade from the ER to the nucleus, ultimately activating three key
662 transcription factors: XBP1s, ATF4, and ATF6. This activation leads to a beneficial adaptive
663 response, upregulating proteostasis genes to restore ER homeostasis (**Fig. 4A**) (69-71). However,
664 ER stress can also trigger maladaptive and deleterious responses, such as the activation of pro-
665 inflammatory and immune gene expression through the TRAF2-mediated activation of AP1
666 (comprised of c-Fos and c-Jun), NF-κB or STAT3 TFs (**Fig. 4A**) (72). Our findings that RBBP5
667 can co-activate XBP1s to regulate the 12h oscillator suggest that RBBP5 is essential for the
668 adaptive UPR TFs-mediated activation of proteostasis genes but is not required for the
669 maladaptive activation of immune genes by immune-regulatory TFs, whose binding motifs are
670 absent from RBBP5 binding sites (**Fig. 2H**).

671 To test this hypothesis, we intraperitoneally injected male *Rbbp5* ^{Flox} and *Rbbp5* ^{LKO} mice with
672 vehicle control or 0.05mg/kg Tu to induce acute ER stress and performed RNA-seq on hepatic
673 transcriptome isolated 8 hours post injection (**Table S5**). This lower dose of Tu was selected for
674 its ability to induce the UPR, but that was significantly less toxic than the more common
675 experimental dose of 1 mg/kg—which is known to elicit hepatocellular death and severe toxicity
676 (73). Western blot analysis confirmed the depletion of RBBP5 and a reduction of H3K4me3 level
677 in the liver of *Rbbp5* ^{LKO} mice (**Fig. 4B**). PCA demonstrated the separation of the four groups on
678 the transcriptome space (**Fig. 4C**). Using an adjusted p value (FDR) of 0.10 as cut-off, we
679 identified 139 and 45 genes significantly induced by Tu in the liver of *Rbbp5* ^{Flox} and *Rbbp5* ^{LKO}
680 mice, respectively, with 21 commonly shared between the two (**Figs. 4D, S7A-G and Table S6**).
681 In *Rbbp5* ^{Flox} mice, these 139 genes are enriched in pathways of proteostasis and immune
682 functions as expected, with pathways of 'response to ER stress' and 'ERAD' among the top two
683 GO terms (**Fig. 4D, E**). By contrast, in *Rbbp5* ^{LKO} mice, these 45 genes are only enriched in
684 immune functions, with proteostasis genes not being significantly induced by Tu (**Fig. 4D, E**). In
685 general, proteostasis genes were induced by Tu to a much greater fold in *Rbbp5* ^{Flox} mice (such
686 as *Creld2*, *Xbp1*, *Hsp90b1*), while the opposite was found for blood coagulation and immune
687 genes in *Rbbp5* ^{LKO} mice (such as *S100a9* and *Fgb*) (**Figs. 4D, E and S7E, F, H**). Further
688 integrating RBBP5 ChIP-seq results, we found that, on average, the ablation of RBBP5 markedly
689 diminished the fold induction by Tu for genes with RBBP5 promoter binding, while it had no effects

690 for those without RBBP5 chromatin recruitment (**Fig. 4D, F**). To rule out the possibility that RBBP5
691 regulates UPR via influencing the upstream ER stressing in the ER, we performed western blot
692 analysis of p-IRE1α and p-PERK in the liver of *Rbbp5* ^{Flox} and *Rbbp5* ^{LKO} mice and did not observe
693 any notable difference in the increase of their phosphorylated level in response to Tu between the
694 two genotypes (**Fig. 4G**).

695 To determine if RBBP5 overexpression is also sufficient to amplify UPR, we tail-vein injected
696 AAV8-TBG-GFP and AAV8-TBG-RBBP5 viruses into wild-type male mice followed by
697 intraperitoneal injection with vehicle control or 0.025mg/kg Tu 30 days later. Thyroxine binding
698 globulin (TBG) promoter is liver-specific and directs RBBP5 transgene expression in hepatocytes
699 (74). qPCR and western blot analysis confirmed an increase of total hepatic expression of RBBP5
700 of ~1.4 fold in AAV8-TBG-RBBP5 group under vehicle control condition (**Fig. 4H, I**). Consequently,
701 RBBP5 hepatic overexpression significantly amplified the UPR of proteostasis genes including
702 *Manf*, *Hspa5* (*BiP*), *Pdia4*, *Hyou1*, and *Syvn1* without affecting the upstream ER stress sensing
703 *(***Fig. 4H, I***)*. In addition, we found that RBBP5 overexpression attenuated the expression of
704 several immune and blood coagulation genes such as *C3*, *Tifa*, *Fgl1* and *Fgb* under ER stress
705 conditions (**Fig. 4I**). Taken together, these results demonstrate that RBBP5 is both necessary and
706 sufficient for the transcriptional regulation of hepatic response to acute proteotoxic stress *in vivo*.
707 RBBP5 activates the expression of proteostasis genes while repressing those involved in immune
708 functions.

709 **RBBP5 protects mice from chronic ER stress-induced hepatic inflammation and steatosis.**

710 Contrary to acute ER stress, chronic ER stress, experimentally reconstituted by repeated injection
711 of Tu, paradoxically leads to feedback-mediated suppression of the UPR signaling, to even below
712 basal levels (73). Proposed mechanisms of this suppression include silencing of the ATF6a
713 branch of UPR, enhancement of mRNA degradation via IRE1-dependent decay (RIDD), and the
714 direct inhibition of UPR stress sensors by the ER chaperone HSPA5 (BiP) (73). To investigate
715 whether RBBP5 also modulates the feedback suppression of UPR under chronic ER stress
716 conditions, we repeatedly intraperitoneally injected male *Rbbp5* ^{Flox} and *Rbbp5* ^{LKO} mice with
717 vehicle control or 0.025mg/kg Tu for six consecutive days and harvested liver tissues 24 hours
718 after the last injection for analysis (**Fig. 5A**). Western blot analysis revealed attenuation of p-
719 IRE1α and ATF4 level in both *Rbbp5* ^{Flox} and *Rbbp5* ^{LKO} mice with repeated Tu injection (**Fig. 5B**).
720 In agreement with the Western blot result, qPCR analysis also confirmed the downregulation of
721 proteostasis genes *Atf4*, *Hyou1*, and *Manf* in both mice under chronic ER stress condition (**Fig.
722 5C**). By contrast, compared to *Rbbp5* ^{Flox} mice, the expression of pro-inflammatory cytokine genes
723 *Il1α* and *Il1b* were higher in Tu-injected *Rbbp5* ^{LKO} mice, consistent with higher levels of p-IRE1α
724 and p-c-Jun (Ser73) observed in *Rbbp5* ^{LKO} mice (**Fig. 5B, C**). The persistent elevated levels of
725 p-IRE1α/p-c-JUN and pro-inflammatory cytokine gene expression in *Rbbp5* ^{LKO} mice suggest that
726 these mice exhibit heightened susceptability to Tu-induced ER stress and inflammation. In
727 summary, our results indicate that while wild-type mice can sustain persistent cycles of UPR
728 activation and deactivation in response to ER stress, as previously described (73), the loss of
729 RBBP5 disrupts this balance. Although RBBP5-deficient mice retain the ability to attenuate UPR,
730 they are unable to properly activate it. Consequently, *Rbbp5* ^{LKO} mice exhibit consistently lower
731 expression of adaptive proteostasis genes under ER stress condition, leading to heightened
732 proteotoxic stress and chronic inflammation likely via activating the p-IRE1α-TRAF2-AP1
733 signaling cascade.

734 Both chronic ER stress and inflammation can result in hepatic steatosis (75-78). We therefore
735 performed Oil Red O staining, which stained all neutral lipids, on liver tissues from *Rbbp5* ^{Flox} and
736 *Rbbp5* ^{LKO} mice after repeated vehicle or Tu injection. *Rbbp5* ^{LKO} mice liver displayed an increased
737 number of lipid droplets and total lipid content, compared to wild-type counterparts under both

basal and chronic ER stress conditions (**Fig. 5D**). Our data revealed that RBBP5 protects mice from chronic ER stress-induced hepatic inflammation and steatosis.

Loss of RBBP5 compromises the cell-autonomous transcriptional response to proteotoxic stress and nutrient-deprivation, resulting in impaired autophagy and reduced cell survival.

To determine whether RBBP5 regulates transcriptional responses to proteotoxic stress in a cell-autonomous manner beyond the liver, we examined MEFs, which exhibit both a robust cell-autonomous XBP1s-dependent 12h oscillator and strong transcriptional responses to proteotoxic stress (17,18,21,79). *Rbbp5* mRNA expression was induced by Tu (**Fig. 6A**), and transient knockdown of RBBP5 using siRNA (**Fig. S8A**) significantly dampened the UPR of proteostasis gene expressions in response to Tu, mirroring the effects observed with XBP1s knockdown (**Fig.6A**). Similarly, knocking down ASH2L also markedly dampened the UPR, whereas knocking down SETD1A, one of the H3K4me3 methyltransferases in the SET1/COMPASS complex, had only modest effects, which were likely due to redundancy among the many H3K4me3 methyltransferases that exist (**Fig. S8B**). As a negative control, we further knocked down both GCN5 and PCAF, proteins that function to write H3K9Ac as subunits in two distinct histone acetyltransferase (HAT) complexes, SAGA (Spt-Ada-Gcn5 acetyltransferase) and ATAC (Ada2a-containing) (80-82) and found it had no effects on the induction of *Xbp1* and *Manf* expression in response to ER stress (**Fig. 6B**). The lack of effects on UPR for HAT subunits is consistent with the absence of ~12h rhythms of both H3K9Ac and H3K27Ac levels around the promoter of ~12h proteostasis genes in mouse liver (**Fig. 1A, B**). ChIP-qPCR analysis confirmed a gradual, temporal increase in the recruitment of RBBP5 to the proximal promoters of select proteostasis genes in response to ER stress, concomitant with an increase in promoter-proximal H3K4me3 levels (**Fig. 6C**). Since XBP1s is the major TF driving UPR, we further performed IF on XBP1s and RBBP5 in MEFs and found a strong recruitment of RBBP5 to XBP1s in response to ER stress (**Fig. 6D, E**).

To broadly assess the function of RBBP5 in the transcription regulation of proteotoxic stress response, we utilized orthogonal approaches to both deplete RBBP5 expression and trigger cellular stress. We took advantage of our homozygous *Rbbp5* ^{Flox} mice by crossing them with homozygous ROSA26 Cre-ERT2 mice, then isolated and immortalized primary MEFs from homozygous F2 embryos (**Fig. S8C**). Treating these *Rbbp5* (flox/flox); ROSA26 Cre-ERT2 (+/+) MEFs with tamoxifen for 7 days resulted in the complete deletion of both floxed *Rbbp5* alleles (**Fig. S8D**) and a subsequent ~90% reduction in RBBP5 protein and a reduction of H3K4me3 level (**Fig. 6F**). The remaining RBBP5 protein is likely extremely long-lived and remains stable even after the deletion of underlying coding genes. To trigger ER stress, we used a different stimulus: Dithiothreitol (DTT), which disrupts protein disulfide formation in the ER (83,84). Similar to Tu, RBBP5 depletion significantly dampened the induction of proteostasis gene expression in response to DTT (**Fig. 6G**).

Next, we tested two additional proteotoxic stressors that are more physiologically relevant: leucine deprivation to simulate amino acid restriction, and a more severe nutrient deprivation stress by culturing cells in Earle's Balanced Salt Solution (EBSS) for 16 hours. Both treatments not only trigger UPR but also activate the broader integrated stress response (ISR), resulting in the induction of autophagy (85). RBBP5 depletion impaired the transcriptional response to both leucine deprivation and EBSS, leading to a reduced induction of autophagy-promoting genes (**Fig. 7A**). Transcriptome profiling by RNA-seq confirmed the globally defective adaptive stress response to nutrient deprivation (EBSS) in the absence of RBBP5, where only 327 out of 2,351 genes can still be induced (**Figs. 7B-D, S8E, and Table S7, 8**). To investigate the physiological consequence of RBBP5 deletion, we quantified the autophagic flux by utilizing a tandem LC3 reporter mCherry-GFP-LC3 where an increase in the number of red-fluorescent cytosolic puncta

786 indicates increased autolysosome formation and autophagic flux (**Fig. 7E**) (85). Consistent with
787 the qPCR results, RBBP5 depleted MEFs failed to induce a robust general autophagy in response
788 to leucine deprivation and further exhibited lower basal level of autophagic flux (**Figs. 7F and**
789 **S8F**). Western blot analysis of p62/SQSTM1, a marker of autophagic flux due to its degradation
790 during autophagy (86), showed a significant reduction in wild-type, but not RBBP5 depleted cells
791 following leucine deprivation, thus confirming the defective autophagy phenotype associated with
792 RBBP5 depletion (**Fig. S8G, H**). Since prolonged nutrient deprivation, such as 16h of EBSS
793 treatment, can robustly induce both general autophagy and autophagy of the ER (ER-phagy) (87),
794 we further measured ER-phagy by utilizing a previously published ER-phagy reporter system
795 where a stably expressed ER-targeting mCherry-RAMP4 fusion is cleaved to free mCherry during
796 starvation-induced ER-phagy (29) (**Fig. 7G**). As shown in **Fig. 7H, I**, RBBP5 depletion prevented
797 the cleavage of mCherry in response to EBSS, indicating an impaired ER-phagy. Western blot
798 analysis of p62/SQSTM1 further showed undetectable levels in wild-type cells following EBSS
799 treatment, whereas a significant level remained in RBBP5 depleted cells under the same
800 conditions, thus confirming a reduction of the general autophagy in RBBP5 depleted cells in
801 response to EBSS (**Fig. 7H**). Consistent with weakened stress response and impaired autophagy,
802 RBBP5 depleted MEFs displayed reduced cell survival under nutritional stress (**Fig. S8I**). Taken
803 together, our results demonstrate that RBBP5 is indispensable for regulating the cell-autonomous
804 transcriptional responses to various proteotoxic stresses as a core subunit of the H3K4me3-
805 writing COMPASS complex.

806 **Proximity labeling reveals H3K4me-associated proteomic architecture of the proteostatic**
807 **stress response.**

808 H3K4me3 is widely recognized as an active promoter mark, but its precise role in transcriptional
809 regulation remains a subject of debate. Initially, it was believed that H3K4me3 facilitated
810 transcription initiation by recruiting the RNAPII preinitiation complex (88), However, recent
811 evidence suggests that H3K4me3 primarily regulates RNAPII pause-release and contributes to
812 transcriptional elongation, likely through the recruitment of Integrator Complex subunit 11 (INTS11)
813 (58,59). This discrepancy may stem from the context-specific functions of H3K4me3 in recruiting
814 different transcriptional regulators across different biological processes (89). To shed light on the
815 potential mechanisms by which H3K4me3 modulates proteostasis stress response, we performed
816 quantitative TurboID-based proximity labeling in MEFs (in triplicates per condition), utilizing anti-
817 H3K4me3 antibody (with anti-IgG as negative control) followed by recombinant protein A-TurboID
818 labeling in isolated nuclei of MEFs before (T=0h) and 2.5h and 8h after ER stress induction by Tu
819 (**Figs. 8A, S9A**) (47). While the total level of H3K4me3 remains largely unchanged during ER
820 stress (**Fig. 8B**), we identified a total of 239 proteins ($p<0.1$) whose recruitment to H3K4me3
821 peaked at 8h post Tu treatment (**Table S9**). Pathway analysis of these 239 proteins revealed
822 expected enrichment of COMPASS subunits (**Figs. 8C, S9B, C**), RNAPII subunits (**Fig. S9D**), as
823 well as previously identified Integrator Complex subunits (such as INTS11) (**Fig. S9E**). The
824 previously identified H3K4me3 demethylase KDM5A (59) revealed a much more constant
825 recruitment to H3K4me3 during ER stress, with only a slight increase at 8h after ER stress
826 induction (**Fig. S9C**).

827 Besides previously identified H3K4me3 writer/eraser/readers, we also revealed strong
828 enrichment of SWI/SNF chromatin remodelers on H3K4me3 peaking at 8h after ER stress
829 induction (**Fig. 8C, D**). These include BAF-specific (ARID1A/B), PBAF-specific (ARID2, PBRM1
830 and BRD7) and shared subunits (SMARCD1/2/3 and SMARCC2) (**Fig. 8C, D**) (90). The timing of
831 SWI/SNF recruitment to H3K4me3 during ER stress closely parallels that of COMPASS and
832 Integrator subunits but lags behind RNAPII subunits (**Fig. 8E**). This temporal pattern suggests
833 that SWI/SNF might potentially play a role in facilitating transcriptional elongation during stress-
834 induced gene activation.

To uncover further evidence supporting the recruitment of SWI/SNF to H3K4me3 during proteostatic stress, we turned back to the hepatic 12h oscillator and examined the temporal expression and cistrome of SWI/SNF subunits in mouse liver. Intriguingly, even before our discovery of the hepatic 12h oscillator in 2017, we had previously reported the 12h rhythmic expression of nuclear PBRM1 (BAF180), ARID2 (BAF200), and SMARCA4 (BRG1) proteins in wild-type mouse liver (36), though at the time, we were unaware of their potential implications in proteostasis control. To validate the hepatic 12h expression of nuclear PBRM1 (BAF180), we performed western blot analysis and confirmed its rhythmic peaks at CT10 and CT22 (**Fig. S10A**). Next, we conducted a post-hoc analysis of our previously published hepatic BAF180 ChIP-seq datasets at CT22, using two different antibodies (Bethyl and Active Motif) (35), and compared them with RBBP5 and H3K4me3 cistromes. Globally, genes with promoter-proximal BAF180 binding (±1 kb from the TSS) were significantly enriched in proteostasis-related pathways, including ER stress, autophagy, and proteolysis (**Fig. 8F, G**). Concordantly, we observed co-enrichment of BAF180, RBBP5, and H3K4me3 at the promoter regions of the 6,451 genes identified in **Fig. 1C,** with a strong positive correlation between their binding intensities on these genes (**Figs. 8H, S10B, C**). Although the causal relationship between SWI/SNF subunits and proteostasis gene expression remains to be determined, our collective findings in both MEFs and liver establish both COMPASS and SWI/SNF as critical components of the chromatin landscape governing dynamic proteostasis gene regulation.

Reduced RBBP5 expression is associated with aging in mice and hepatic steatosis in humans.

The roles of RBBP5 in diseases are incompletely understood (56,91). Since the decline of proteostasis and stress response is causally associated with both aging and metabolic diseases (92-95), we aim to uncover potential implications of RBBP5 in these two processes. Intriguingly, in a recent study, RBBP5 (and DPY30) is predicted to be a positive regulator of maximum lifespan across 26 different species, with its major effect predicted to be related to liver (96). Consistent with this prediction, an overall reduction of *Rbbp5* mRNA level is observed in the liver of aging mice (97), largely concordant with the expression dynamics of 97 stress response genes (those genes exhibiting 12h expression, directly bound by RBBP5 and can be induced by ER stress) (**Fig. 9A**).

Leveraging human gene-derived correlations across tissues (GD-CAT) dataset (98), we identified in human liver, RBBP5 expression is positively correlated with those involved in proteostasis (such as ribosome biogenesis, translation regulation) and mRNA metabolism (mRNA splicing and processing) and negatively associated with those implicated in immune response (acute phase response, complement activity, and immunoglobin activity) (**Fig. S11**). These results are in line with our RNA-seq and ChIP-seq data obtained from *Rbbp5* ^{Flox} and *Rbbp5* ^{LKO} mice (**Figs. 2C, 3I, 4D**). In humans with NAFLD/MAFLD (99), compared to healthy obese, RBBP5 mRNA level is significantly reduced in steatosis subjects (**Fig. 9B**), concordant with reduced stress gene expression in the same cohorts (**Fig. 9C-F**). Overall, a positive correlation between *Rbbp5* and the eigengene expression of stress response genes [eigengene (100) is the principle component of 97 stress response genes expression in each subject] is observed across all subjects (**Fig. 9D**). Collectively, these data suggest that the downregulation of *Rbbp5* and proteostatic stress response genes expression is associated with aging and MAFLD in mice and humans, respectively.

Discussion:

While the epigenetic landscape of the mammalian ~24h circadian clock was well-studied (54,101-104), the epigenome of the mammalian ~12h ultradian oscillator remains completely unexplored. In this study, we uncovered that unlike the circadian clock, which was predominantly regulated by

histone acetyltransferase (HAT) (35,105,106) and histone deacetylase (HDAC) (103,107,108), the epigenome of the 12h oscillator is marked by COMPASS-mediated histone methylation, specifically H3K4me3 at the proximal promoters. Loss of one of the essential subunits of COMPASS, RBBP5, abolished more than 90% of the hepatic ~12h transcriptome, while having no effects on the core circadian clock. Knocking down RBBP5 in MEFs further dampened the cell-autonomous 12h oscillations, but not the circadian rhythms. We further expanded our findings to the epigenetic regulation of response to acute and chronic proteotoxic stress and found both increased RBBP5 promoter recruitment and H3K4me3 level are associated with the transcription activation of adaptive stress response genes. Subsequently, depletion of RBBP5 significantly dampened the adaptive transcriptional responses to various proteotoxic stresses.

In our study, we uncovered distinct roles for H3K4me3 and H3K9Ac/H3K27Ac in regulating the 12h oscillator and transcriptional responses to acute proteotoxic stress. While all three histone modifications—H3K4me3, H3K9Ac, and H3K27Ac—are traditionally linked to transcriptional activation (81,82,109), our findings suggest that H3K9Ac and H3K27Ac are dispensable for the transcriptional regulation of proteostasis under both basal (the 12h oscillator) and stress conditions. Interestingly, recent research by (110) demonstrated that among various epigenetic marks associated with transcriptional activation, the installation of H3K4me3 at promoters resulted in the most potent transcriptional activation. This not only underscores the causal role of H3K4me3 in gene activation but also highlights the differential impacts of specific histone modifications on transcription. We speculate that among the many histone modifications, H3K4me3 has been evolutionarily selected as the primary epigenetic modification for stress response due to its ability to trigger the most robust gene activation, thereby providing a rapid adaptive advantage under adverse environmental conditions. Future investigations are needed to further test this hypothesis.

The precise role of H3K4me3 in transcriptional regulation remains a topic of debate. Recent evidence suggests that H3K4me3 positively contributes to transcriptional elongation by regulating the pause-release of RNAP II, likely through the recruitment of the Integrator subunit INST11 (89). Our H3K4me3 proximity labeling not only supports this finding but also unexpectedly reveals increased recruitment of the SWI/SNF complex to H3K4me3 during the UPR in MEFs. Additionally, we confirmed the co-occurrence of RBBP5, H3K4me3, and the PBAF subunit BAF180 in chromatin binding in vivo in mouse liver. Interestingly, the temporal dynamics of SWI/SNF recruitment to H3K4me3 coincide with the recruitment of the Integrator complex but occur after the initial increase in RNAP II subunits, which are likely involved in transcription initiation immediately following stress. This suggests that contrary to the widely accepted view that SWI/SNF primarily facilitates transcription initiation by increasing chromatin accessibility and transcription factor binding to promoter, it may also play a crucial yet underexplored role in transcription elongation. Although the literature on this aspect is rather limited, some earlier studies hint at this possibility (111,112). Future research is needed to firmly establish a causal relationship between SWI/SNF function, 12h oscillator regulation, and the proteostasis stress response, as well as to uncover the underlying molecular mechanisms.

The physiological and pathological roles of mammalian COMPASS subunits, particularly RBBP5, remain incompletely understood (91). While extensive research has primarily focused on their contributions to organogenesis, early development, and neurodevelopmental disorders, our study significantly broadens the scope of RBBP5's physiological roles by uncovering its involvement in proteostasis and hepatic metabolism. This expansion not only advances our understanding of RBBP5's function but also opens new avenues for exploring its broader impact on cellular and systemic processes. Of particular interest is a recent study that identified heterozygous loss-of-function mutations in *RBBP5* in humans, which were primarily linked to neurodevelopmental disorders (113). This finding raises intriguing questions about the full

spectrum of RBBP5's physiological roles. Given our discovery of RBBP5's involvement in metabolic regulation, it is tempting to hypothesize that individuals with RBBP5 loss-of-function mutations may also exhibit metabolic defects. Such a connection would have significant implications, suggesting that RBBP5 plays a multifaceted role in maintaining both neural and metabolic homeostasis. Future research should investigate whether these mutations influence metabolic pathways, potentially contributing to a broader spectrum of clinical symptoms in affected individuals. This line of inquiry could ultimately lead to a deeper understanding of how COMPASS subunits like RBBP5 integrate signals across different tissues to maintain overall physiological balance.

Finally, we propose that the 12h oscillator serves as an effective 'discovery tool' for uncovering previously unknown mechanisms of proteostasis regulation. By leveraging this approach, we recently identified a novel XBP1s-SON axis, which links nuclear speckle LLPS dynamics with the UPR (26). Herein, using a similar approach, we identified RBBP5 as an epigenetic regulator of proteostasis. We believe that continued exploration of the 12h oscillator will unveil further hidden principles governing proteostasis.

Acknowledgements:

We would like to thank Dr. Sebastien Gingras (University of Pittsburgh, Department of Immunology) for the design of the targeting strategy and identification of the founders carrying the properly targeted Rbbp5-flox allele. We would like to thank Chunming Bi and Zhaohui Kou of the Mouse Embryo Services Core (University of Pittsburgh, Department of Immunology) for microinjection of zygotes and production of Rbbp5-flox founder mice. We would also like to thank Dr. Heather Ballance, Dr. Naveen GV Kumar, Saad Irfan, C. Dupont, Dr. Bugra Zengin and Casey Edwards for assistance with mice colony maintenance, dissection, intraperitoneal injection and genotyping. We would also like to thank Dr. Michiel Vermeulen for kindly sharing the pK19HispATurbo plasmid. For time course transcriptome study, the library generation was performed in the Health Sciences Sequencing Core at UPMC Children's Hospital of Pittsburgh, Rangos Research Center. Services and instruments used in this project were graciously supported, in part, by the University of Pittsburgh, the Office of the Senior Vice Chancellor for Health Sciences, the Department of Pediatrics, the Institute for Precision Medicine, and the Richard K Mellon Foundation for Pediatric Research.

W.D. was supported by fellowship F31 AG080998 through NIA. B. Zhu was supported by grants 1DP2GM140924 and 1R21AG071893 through the NIH, and a grant from Richard King Mellon foundation. This research was supported in part by the University of Pittsburgh Center for Research Computing through the resources provided. Specifically, this work used the HTC cluster, which is supported by NIH award number S10OD028483. This research project was supported in part by the Pittsburgh Liver Research Centre supported by NIH/NIDDK Digestive Disease Research Core Center grant P30DK120531.

Author contributions:

Conceptualization, B.Z.; Methodology, M.J. and B.Z.; Investigation, S.K., M.S., W.D., A.C., H.L., H.W., A.P., I.S., S.L., Y.P., L.L., J.J.L., and B.Z.; Writing – Original Draft, B.Z.; Writing – Review & Editing, all authors; Funding Acquisition, S.L., and B.Z.; Resources, M.J., J.H.L and B.Z.; Supervision, M.J., J.H.L and B.Z.

Disclosure and competing interests:

The authors have no competing interests to declare.

Data availability:

977 All raw and processed sequencing data generated in this study have been submitted to the NCBI
978 Gene Expression Omnibus (GEO; http://www.ncbi.nlm.nih.gov/geo/) under accession numbers:
979 GSE276155, GSE276157 and GSE276159. All data needed to evaluate the conclusions in the
980 paper are present in the paper and/or the Supplementary Materials.

981 **References:**

982 1. Labbadia, J. and Morimoto, R.I. (2015) The Biology of Proteostasis in Aging and
983 Disease. *Annual Review of Biochemistry*, **84**, 435-464.

984 2. Buttgereit, F. and Brand, M.D. (1995) A hierarchy of ATP-consuming processes in
985 mammalian cells. *Biochemical Journal*, **312**, 163-167.

986 3. Zhao, L. and Ackerman, S.L. (2006) Endoplasmic reticulum stress in health and disease.
987 *Current Opinion in Cell Biology*, **18**, 444-452.

988 4. Klaips, C.L., Jayaraj, G.G. and Hartl, F.U. (2018) Pathways of cellular proteostasis in
989 aging and disease. *J Cell Biol*, **217**, 51-63.

990 5. Martinez, G., Duran-Aniotz, C., Cabral-Miranda, F., Vivar, J.P. and Hetz, C. (2017)
991 Endoplasmic reticulum proteostasis impairment in aging. *Aging Cell*, **16**, 615-623.

992 6. Taylor, R.C. and Hetz, C. (2020) Mastering organismal aging through the endoplasmic
993 reticulum proteostasis network. *Aging Cell*, **19**, e13265.

994 7. Costa-Mattioli, M. and Walter, P. (2020) The integrated stress response: From
995 mechanism to disease. *Science*, **368**, eaat5314.

996 8. Hetz, C., Zhang, K. and Kaufman, R.J. (2020) Mechanisms, regulation and functions of
997 the unfolded protein response. *Nature Reviews Molecular Cell Biology*, **21**, 421-438.

998 9. Richter, K., Haslbeck, M. and Buchner, J. (2010) The heat shock response: life on the
999 verge of death. *Mol Cell*, **40**, 253-266.

1000 10. Ron, D. and Walter, P. (2007) Signal integration in the endoplasmic reticulum unfolded
1001 protein response. *Nature Reviews Molecular Cell Biology*, **8**, 519-529.

1002 11. Balch, W.E., Morimoto, R.I., Dillin, A. and Kelly, J.W. (2008) Adapting proteostasis for
1003 disease intervention. *Science*, **319**, 916-919.

1004 12. Ballance, H. and Zhu, B. (2021) Revealing the hidden reality of the mammalian 12-h
1005 ultradian rhythms. *Cellular and Molecular Life Sciences*.

1006 13. Asher, G. and Zhu, B. (2022) Beyond circadian rhythms: Emerging roles of ultradian
1007 rhythms in control of liver functions. *Hepatology*, **n/a**.

1008 14. Scott, M.R., Zong, W., Ketchesin, K.D., Seney, M.L., Tseng, G.C., Zhu, B. and McClung,
1009 C.A. (2023) Twelve-hour rhythms in transcript expression within the human dorsolateral
1010 prefrontal cortex are altered in schizophrenia. *PLOS Biology*, **21**, e3001688.

15. Zhu, B., Liu, S., David, N.L., Dion, W., Doshi, N.K., Siegel, L.B., Amorim, T., Andrews, R.E., Kumar, G.N., Irfan, S. *et al.* (2023) Evidence for conservation of a primordial 12-hour ultradian gene program in humans. *bioRxiv*, 2023.2005.2002.539021.

16. Zhu, B., Liu, S., David, N.L., Dion, W., Doshi, N.K., Siegel, L.B., Amorim, T., Andrews, R.E., Kumar, G.V.N., Li, H. *et al.* (2024) Evidence for ~12-h ultradian gene programs in humans. *npj Biological Timing and Sleep*, **1**, 4.

17. Dion, W., Ballance, H., Lee, J., Pan, Y., Irfan, S., Edwards, C., Sun, M., Zhang, J., Zhang, X. and Liu, S. (2022) Four-dimensional nuclear speckle phase separation dynamics regulate proteostasis. *Science Advances*, **8**, eabl4150.

18. Zhu, B., Zhang, Q., Pan, Y., Mace, E.M., York, B., Antoulas, A.C., Dacso, C.C. and O'Malley, B.W. (2017) A cell-autonomous mammalian 12 hr clock coordinates metabolic and stress rhythms. *Cell metabolism*, **25**, 1305-1319. e1309.

19. Meng, H., Gonzales, N.M., Lonard, D.M., Putluri, N., Zhu, B., Dacso, C.C., York, B. and O'Malley, B.W. (2020) XBP1 links the 12-hour clock to NAFLD and regulation of membrane fluidity and lipid homeostasis. *Nature Communications*, **11**, 6215.

20. Meng, H., Gonzales, N.M., Jung, S.Y., Lu, Y., Putluri, N., Zhu, B., Dacso, C.C., Lonard, D.M. and O'Malley, B.W. (2022) Defining the mammalian coactivation of hepatic 12-h clock and lipid metabolism. *Cell Reports*, **38**, 110491.

21. Pan, Y., Ballance, H., Meng, H., Gonzalez, N., Kim, S.-M., Abdurehman, L., York, B., Chen, X., Schnytzer, Y., Levy, O. *et al.* (2020) 12-h clock regulation of genetic information flow by XBP1s. *PLOS Biology*, **18**, e3000580.

22. Asher, G. and Zhu, B. (2022) Beyond circadian rhythms: Emerging roles of ultradian rhythms in control of liver functions. *Hepatology*.

23. Zhu, B., Zhang, Q., Pan, Y., Mace, E.M., York, B., Antoulas, A.C., Dacso, C.C. and O'Malley, B.W. (2017) A Cell-Autonomous Mammalian 12 hr Clock Coordinates Metabolic and Stress Rhythms. *Cell Metab*, **25**, 1305-1319 e1309.

24. Zhu, B. and Liu, S. (2023) Preservation of ~12-hour ultradian rhythms of gene expression of mRNA and protein metabolism in the absence of canonical circadian clock. *bioRxiv*, 2023.2005.2001.538977.

25. Zhang, H., Yahagi, T., Miyamoto, N., Chen, C., Jiang, Q., Qian, P.-Y. and Sun, J. (2025) Circatidal control of gene expression in the deep-sea hot vent shrimp Rimicaris leurokolos. *Proceedings of the Royal Society B: Biological Sciences*, **292**, 20242970.

26. Dion, W., Ballance, H., Lee, J., Pan, Y., Irfan, S., Edwards, C., Sun, M., Zhang, J., Zhang, X., Liu, S. *et al.* (2022) Four-dimensional nuclear speckle phase separation dynamics regulate proteostasis. *Science Advances*, **8**, eabl4150.

27. Shilatifard, A. (2012) The COMPASS family of histone H3K4 methylases: mechanisms of regulation in development and disease pathogenesis. *Annu Rev Biochem*, **81**, 65-95.

1048 28. Wulansari, N., Darsono, W.H.W., Woo, H.J., Chang, M.Y., Kim, J., Bae, E.J., Sun, W.,
1049 Lee, J.H., Cho, I.J., Shin, H. *et al.* (2021) Neurodevelopmental defects and
1050 neurodegenerative phenotypes in human brain organoids carrying Parkinson's disease-
1051 linked DNAJC6 mutations. *Sci Adv*, **7**.

1052 29. Liang, J.R., Lingeman, E., Ahmed, S. and Corn, J.E. (2018) Atlastins remodel the
1053 endoplasmic reticulum for selective autophagy. *J Cell Biol*, **217**, 3354-3367.

1054 30. Quadros, R.M., Miura, H., Harms, D.W., Akatsuka, H., Sato, T., Aida, T., Redder, R.,
1055 Richardson, G.P., Inagaki, Y., Sakai, D. *et al.* (2017) Easi-CRISPR: a robust method for
1056 one-step generation of mice carrying conditional and insertion alleles using long ssDNA
1057 donors and CRISPR ribonucleoproteins. *Genome Biol*, **18**, 92.

1058 31. Pelletier, S., Gingras, S. and Green, D.R. (2015) Mouse genome engineering via
1059 CRISPR-Cas9 for study of immune function. *Immunity*, **42**, 18-27.

1060 32. Xu, J. (2005) Preparation, culture, and immortalization of mouse embryonic fibroblasts.
1061 *Curr Protoc Mol Biol*, **Chapter 28**, Unit 28.21.

1062 33. Zhu, B., Gates, L.A., Stashi, E., Dasgupta, S., Gonzales, N., Dean, A., Dacso, C.C.,
1063 York, B. and O'Malley, B.W. (2015) Coactivator-Dependent Oscillation of Chromatin
1064 Accessibility Dictates Circadian Gene Amplitude via REV-ERB Loading. *Mol Cell*.

1065 34. Malovannaya, A., Lanz, R.B., Jung, S.Y., Bulynko, Y., Le, N.T., Chan, D.W., Ding, C., Shi,
1066 Y., Yucer, N., Krenciute, G. *et al.* (2011) Analysis of the human endogenous coregulator
1067 complexome. *Cell*, **145**, 787-799.

1068 35. Zhu, B., Gates, L.A., Stashi, E., Dasgupta, S., Gonzales, N., Dean, A., Dacso, C.C.,
1069 York, B. and O'Malley, B.W. (2015) Coactivator-Dependent Oscillation of Chromatin
1070 Accessibility Dictates Circadian Gene Amplitude via REV-ERB Loading. *Mol Cell*, **60**,
1071 769-783.

1072 36. Zhu, B., Gates, L.A., Stashi, E., Dasgupta, S., Gonzales, N., Dean, A., Dacso, C.C.,
1073 York, B. and O'Malley, B.W. (2015) Coactivator-dependent oscillation of chromatin
1074 accessibility dictates circadian gene amplitude via REV-ERB loading. *Molecular cell*, **60**,
1075 769-783.

1076 37. Bolger, A.M., Lohse, M. and Usadel, B. (2014) Trimmomatic: a flexible trimmer for
1077 Illumina sequence data. *Bioinformatics*, **30**, 2114-2120.

1078 38. Kim, D., Langmead, B. and Salzberg, S.L. (2015) HISAT: a fast spliced aligner with low
1079 memory requirements. *Nat Methods*, **12**, 357-360.

1080 39. Antoulas, A.C., Zhu, B., Zhang, Q., York, B., O'Malley, B.W. and Dacso, C.C. (2018) A
1081 novel mathematical method for disclosing oscillations in gene transcription: A
1082 comparative study. *PLoS One*, **13**, e0198503.

1083 40. Thaben, P.F. and Westermark, P.O. (2014) Detecting rhythms in time series with RAIN. *J*
1084 *Biol Rhythms*, **29**, 391-400.

1085 41. Liu, S., Obert, C., Yu, Y.P., Zhao, J., Ren, B.G., Liu, J.J., Wiseman, K., Krajacich, B.J.,
1086 Wang, W., Metcalfe, K. *et al.* (2024) Utility analyses of AVITI sequencing chemistry. *BMC*
1087 *Genomics*, **25**, 778.

1088 42. Bolger, A.M., Lohse, M. and Usadel, B. (2014) Trimmomatic: a flexible trimmer for
1089 Illumina sequence data. *Bioinformatics*, **30**, 2114-2120.

1090 43. Dobin, A., Davis, C.A., Schlesinger, F., Drenkow, J., Zaleski, C., Jha, S., Batut, P.,
1091 Chaisson, M. and Gingeras, T.R. (2013) STAR: ultrafast universal RNA-seq aligner.
1092 *Bioinformatics*, **29**, 15-21.

1093 44. Trapnell, C., Williams, B.A., Pertea, G., Mortazavi, A., Kwan, G., van Baren, M.J.,
1094 Salzberg, S.L., Wold, B.J. and Pachter, L. (2010) Transcript assembly and quantification
1095 by RNA-Seq reveals unannotated transcripts and isoform switching during cell
1096 differentiation. *Nature Biotechnology*, **28**, 511-U174.

1097 45. Ge, S.X., Son, E.W. and Yao, R. (2018) iDEP: an integrated web application for
1098 differential expression and pathway analysis of RNA-Seq data. *BMC bioinformatics*, **19**,
1099 1-24.

1100 46. Ramirez, F., Ryan, D.P., Gruning, B., Bhardwaj, V., Kilpert, F., Richter, A.S., Heyne, S.,
1101 Dundar, F. and Manke, T. (2016) deepTools2: a next generation web server for deep-
1102 sequencing data analysis. *Nucleic Acids Res*, **44**, W160-165.

1103 47. Santos-Barriopedro, I., van Mierlo, G. and Vermeulen, M. (2021) Off-the-shelf proximity
1104 biotinylation for interaction proteomics. *Nature Communications*, **12**, 5015.

1105 48. Huang da, W., Sherman, B.T. and Lempicki, R.A. (2009) Systematic and integrative
1106 analysis of large gene lists using DAVID bioinformatics resources. *Nat Protoc*, **4**, 44-57.

1107 49. He, H.H., Meyer, C.A., Shin, H., Bailey, S.T., Wei, G., Wang, Q., Zhang, Y., Xu, K., Ni,
1108 M., Lupien, M. *et al.* (2010) Nucleosome dynamics define transcriptional enhancers.
1109 *Nature Genetics*, **42**, 343-347.

1110 50. Zhu, B. (2020) Decoding the function and regulation of the mammalian 12h-clock.
1111 *Journal of Molecular Cell Biology*.

1112 51. Dasgupta, S., Lonard, D.M. and O'Malley, B.W. (2014) Nuclear receptor coactivators:
1113 master regulators of human health and disease. *Annu Rev Med*, **65**, 279-292.

1114 52. Roeder, R.G. (2005) Transcriptional regulation and the role of diverse coactivators in
1115 animal cells. *FEBS Lett*, **579**, 909-915.

1116 53. Spiegelman, B.M. and Heinrich, R. (2004) Biological control through regulated
1117 transcriptional coactivators. *Cell*, **119**, 157-167.

1118 54. Koike, N., Yoo, S.H., Huang, H.C., Kumar, V., Lee, C., Kim, T.K. and Takahashi, J.S.
1119 (2012) Transcriptional architecture and chromatin landscape of the core circadian clock
1120 in mammals. *Science*, **338**, 349-354.

1121 55. Takahashi, Y.H., Westfield, G.H., Oleskie, A.N., Trievel, R.C., Shilatifard, A. and Skiniotis,
1122 G. (2011) Structural analysis of the core COMPASS family of histone H3K4 methylases
1123 from yeast to human. *Proc Natl Acad Sci U S A*, **108**, 20526-20531.

1124 56. Shilatifard, A. (2012) The COMPASS family of histone H3K4 methylases: mechanisms of
1125 regulation in development and disease pathogenesis. *Annual review of biochemistry*, **81**,
1126 65-95.

1127 57. Qu, Q., Takahashi, Y.H., Yang, Y., Hu, H., Zhang, Y., Brunzelle, J.S., Couture, J.F.,
1128 Shilatifard, A. and Skiniotis, G. (2018) Structure and Conformational Dynamics of a
1129 COMPASS Histone H3K4 Methyltransferase Complex. *Cell*, **174**, 1117-1126.e1112.

1130 58. Hu, S., Song, A., Peng, L., Tang, N., Qiao, Z., Wang, Z., Lan, F. and Chen, F.X. (2023)
1131 H3K4me2/3 modulate the stability of RNA polymerase II pausing. *Cell Research*, **33**,
1132 403-406.

1133 59. Wang, H., Fan, Z., Shliaha, P.V., Miele, M., Hendrickson, R.C., Jiang, X. and Helin, K.
1134 (2023) H3K4me3 regulates RNA polymerase II promoter-proximal pause-release.
1135 *Nature*, **615**, 339-348.

1136 60. Qin, Q., Fan, J., Zheng, R., Wan, C., Mei, S., Wu, Q., Sun, H., Brown, M., Zhang, J.,
1137 Meyer, C.A. *et al.* (2020) Lisa: inferring transcriptional regulators through integrative
1138 modeling of public chromatin accessibility and ChIP-seq data. *Genome Biology*, **21**, 32.

1139 61. Li, Y., Han, J., Zhang, Y., Cao, F., Liu, Z., Li, S., Wu, J., Hu, C., Wang, Y., Shuai, J. *et al.*
1140 (2016) Structural basis for activity regulation of MLL family methyltransferases. *Nature*,
1141 **530**, 447-452.

1142 62. Ruthenburg, A.J., Allis, C.D. and Wysocka, J. (2007) Methylation of lysine 4 on histone
1143 H3: intricacy of writing and reading a single epigenetic mark. *Mol Cell*, **25**, 15-30.

1144 63. Han, J., Li, T., Li, Y., Li, M., Wang, X., Peng, C., Su, C., Li, N., Li, Y., Xu, Y. *et al.* (2019)
1145 The internal interaction in RBBP5 regulates assembly and activity of MLL1
1146 methyltransferase complex. *Nucleic Acids Research*, **47**, 10426-10438.

1147 64. Antoulas, A.C., Zhu, B., Zhang, Q., York, B., O'Malley, B.W. and Dacso, C.C. (2018) A
1148 novel mathematical method for disclosing oscillations in gene transcription: a
1149 comparative study. *PLoS One*, **13**, e0198503.

1150 65. Zhu, B. and Liu, S. (2023) Preservation of ∼12-h ultradian rhythms of gene expression of
1151 mRNA and protein metabolism in the absence of canonical circadian clock. *Frontiers in*
1152 *Physiology*, **14**.

1153 66. Hughes, M.E., DiTacchio, L., Hayes, K.R., Vollmers, C., Pulivarthy, S., Baggs, J.E.,
1154 Panda, S. and Hogenesch, J.B. (2009) Harmonics of circadian gene transcription in
1155 mammals. *PLoS Genet*, **5**, e1000442.

1156 67. van der Veen, D.R. and Gerkema, M.P. (2017) Unmasking ultradian rhythms in gene
1157 expression. *The FASEB Journal*, **31**, 743-750.

1158 68. Zhang, E.E., Liu, A.C., Hirota, T., Miraglia, L.J., Welch, G., Pongsawakul, P.Y., Liu, X.,
1159 Atwood, A., Huss, J.W., 3rd, Janes, J. *et al.* (2009) A genome-wide RNAi screen for
1160 modifiers of the circadian clock in human cells. *Cell*, **139**, 199-210.

1161 69. Walter, P. and Ron, D. (2011) The unfolded protein response: from stress pathway to
1162 homeostatic regulation. *Science*, **334**, 1081-1086.

1163 70. Metcalf, M.G., Higuchi-Sanabria, R., Garcia, G., Tsui, C.K. and Dillin, A. (2020) Beyond
1164 the cell factory: Homeostatic regulation of and by the UPR^{ER}. *Science*
1165 *Advances*, **6**, eabb9614.

1166 71. Wiseman, R.L., Mesgarzadeh, J.S. and Hendershot, L.M. (2022) Reshaping
1167 endoplasmic reticulum quality control through the unfolded protein response. *Molecular*
1168 *Cell*, **82**, 1477-1491.

1169 72. So, J.S. (2018) Roles of Endoplasmic Reticulum Stress in Immune Responses. *Mol*
1170 *Cells*, **41**, 705-716.

1171 73. Rutkowski, D.T., Wu, J., Back, S.H., Callaghan, M.U., Ferris, S.P., Iqbal, J., Clark, R.,
1172 Miao, H., Hassler, J.R., Fornek, J. *et al.* (2008) UPR pathways combine to prevent
1173 hepatic steatosis caused by ER stress-mediated suppression of transcriptional master
1174 regulators. *Dev Cell*, **15**, 829-840.

1175 74. Yan, Z., Yan, H. and Ou, H. (2012) Human thyroxine binding globulin (TBG) promoter
1176 directs efficient and sustaining transgene expression in liver-specific pattern. *Gene*, **506**,
1177 289-294.

1178 75. Guo, B. and Li, Z. (2014) Endoplasmic reticulum stress in hepatic steatosis and
1179 inflammatory bowel diseases. *Frontiers in Genetics*, **5**.

1180 76. Ajoolabady, A., Kaplowitz, N., Lebeaupin, C., Kroemer, G., Kaufman, R.J., Malhi, H. and
1181 Ren, J. (2023) Endoplasmic reticulum stress in liver diseases. *Hepatology*, **77**, 619-639.

1182 77. Gong, H., He, Q., Zhu, L., Feng, Z., Sun, M., Jiang, J., Yuan, X., Shen, Y. and Di, J.
1183 (2024) Associations between systemic inflammation indicators and nonalcoholic fatty
1184 liver disease: evidence from a prospective study. *Frontiers in Immunology*, **15**.

1185 78. Gehrke, N. and Schattenberg, J.M. (2020) Metabolic Inflammation—A Role for Hepatic
1186 Inflammatory Pathways as Drivers of Comorbidities in Nonalcoholic Fatty Liver Disease?
1187 *Gastroenterology*, **158**, 1929-1947.e1926.

1188 79. Dion, W., Tao, Y., Chambers, M., Zhao, S., Arbuckle, R.K., Sun, M., Kubra, S., Nie, Y.,
1189 Ye, M., Larsen, M.B. *et al.* (2024) Nuclear speckle rejuvenation alleviates
1190 proteinopathies at the expense of YAP1. *bioRxiv*, 2024.2004.2018.590103.

1191 80. Jin, Q., Yu, L.R., Wang, L., Zhang, Z., Kasper, L.H., Lee, J.E., Wang, C., Brindle, P.K.,
1192 Dent, S.Y. and Ge, K. (2011) Distinct roles of GCN5/PCAF-mediated H3K9ac and
1193 CBP/p300-mediated H3K18/27ac in nuclear receptor transactivation. *Embo j*, **30**, 249-
1194 262.

1195 81. Gates, L.A., Foulds, C.E. and O'Malley, B.W. (2017) Histone Marks in the 'Driver's Seat':
1196 Functional Roles in Steering the Transcription Cycle. *Trends Biochem Sci*, **42**, 977-989.

1197 82. Gates, L.A., Shi, J., Rohira, A.D., Feng, Q., Zhu, B., Bedford, M.T., Sagum, C.A., Jung,
1198 S.Y., Qin, J., Tsai, M.J. *et al.* (2017) Acetylation on histone H3 lysine 9 mediates a switch
1199 from transcription initiation to elongation. *J Biol Chem*, **292**, 14456-14472.

1200 83. Higa, A., Taouji, S., Lhomond, S., Jensen, D., Fernandez-Zapico, M.E., Simpson, J.C.,
1201 Pasquet, J.M., Schekman, R. and Chevet, E. (2014) Endoplasmic reticulum stress-
1202 activated transcription factor ATF6α requires the disulfide isomerase PDIA5 to modulate
1203 chemoresistance. *Mol Cell Biol*, **34**, 1839-1849.

1204 84. G, G. and Singh, J. (2022) Dithiothreitol causes toxicity in C. elegans by modulating the
1205 methionine–homocysteine cycle. *eLife*, **11**, e76021.

1206 85. Pakos-Zebrucka, K., Koryga, I., Mnich, K., Ljujic, M., Samali, A. and Gorman, A.M.
1207 (2016) The integrated stress response. *EMBO Rep*, **17**, 1374-1395.

1208 86. Bjørkøy, G., Lamark, T., Pankiv, S., Øvervatn, A., Brech, A. and Johansen, T. (2009)
1209 Monitoring autophagic degradation of p62/SQSTM1. *Methods Enzymol*, **452**, 181-197.

1210 87. Liang, J.R., Lingeman, E., Luong, T., Ahmed, S., Muhar, M., Nguyen, T., Olzmann, J.A.
1211 and Corn, J.E. (2020) A Genome-wide ER-phagy Screen Highlights Key Roles of
1212 Mitochondrial Metabolism and ER-Resident UFMylation. *Cell*, **180**, 1160-1177.e1120.

1213 88. Gates, L.A., Shi, J., Rohira, A.D., Feng, Q., Zhu, B., Bedford, M.T., Sagum, C.A., Jung,
1214 S.Y., Qin, J. and Tsai, M.-J. (2017) Acetylation on histone H3 lysine 9 mediates a switch
1215 from transcription initiation to elongation. *Journal of Biological Chemistry*, **292**, 14456-
1216 14472.

1217 89. Wang, H. and Helin, K. (2025) Roles of H3K4 methylation in biology and disease. *Trends*
1218 *in Cell Biology*, **35**, 115-128.

1219 90. Hodges, C., Kirkland, J.G. and Crabtree, G.R. (2016) The Many Roles of BAF
1220 (mSWI/SNF) and PBAF Complexes in Cancer. *Cold Spring Harb Perspect Med*, **6**.

1221 91. Cenik, B.K. and Shilatifard, A. (2021) COMPASS and SWI/SNF complexes in
1222 development and disease. *Nature Reviews Genetics*, **22**, 38-58.

1223 92. Ghemrawi, R., Battaglia-Hsu, S.F. and Arnold, C. (2018) Endoplasmic Reticulum Stress
1224 in Metabolic Disorders. *Cells*, **7**.

1225 93. Mohan, S., R, P.R.M., Brown, L., Ayyappan, P. and G, R.K. (2019) Endoplasmic
1226 reticulum stress: A master regulator of metabolic syndrome. *European Journal of*
1227 *Pharmacology*, **860**, 172553.

1228 94. Kourtis, N. and Tavernarakis, N. (2011) Cellular stress response pathways and ageing:
1229 intricate molecular relationships. *The EMBO journal*, **30**, 2520-2531.

95. Chen, K., Shen, W., Zhang, Z., Xiong, F., Ouyang, Q. and Luo, C. (2020) Age-dependent decline in stress response capacity revealed by proteins dynamics analysis. *Scientific Reports*, **10**, 15211.

96. Lu, J.Y., Simon, M., Zhao, Y., Ablaeva, J., Corson, N., Choi, Y., Yamada, K.Y.H., Schork, N.J., Hood, W.R., Hill, G.E. *et al.* (2022) Comparative transcriptomics reveals circadian and pluripotency networks as two pillars of longevity regulation. *Cell Metabolism*, **34**, 836-856.e835.

97. Almanzar, N., Antony, J., Baghel, A.S., Bakerman, I., Bansal, I., Barres, B.A., Beachy, P.A., Berdnik, D., Bilen, B., Brownfield, D. *et al.* (2020) A single-cell transcriptomic atlas characterizes ageing tissues in the mouse. *Nature*, **583**, 590-595.

98. Zhou, M., Tamburini, I., Van, C., Molendijk, J., Nguyen, C.M., Chang, I.Y.-Y., Johnson, C., Velez, L.M., Cheon, Y., Yeo, R. *et al.* (2024) Leveraging inter-individual transcriptional correlation structure to infer discrete signaling mechanisms across metabolic tissues. *eLife*, **12**, RP88863.

99. Ahrens, M., Ammerpohl, O., von Schönfels, W., Kolarova, J., Bens, S., Itzel, T., Teufel, A., Herrmann, A., Brosch, M., Hinrichsen, H. *et al.* (2013) DNA Methylation Analysis in Nonalcoholic Fatty Liver Disease Suggests Distinct Disease-Specific and Remodeling Signatures after Bariatric Surgery. *Cell Metabolism*, **18**, 296-302.

100. Langfelder, P. and Horvath, S. (2007) Eigengene networks for studying the relationships between co-expression modules. *BMC Systems Biology*, **1**, 54.

101. Masri, S., Kinouchi, K. and Sassone-Corsi, P. (2015) Circadian clocks, epigenetics, and cancer. *Curr Opin Oncol*, **27**, 50-56.

102. Takahashi, J.S. (2017) Transcriptional architecture of the mammalian circadian clock. *Nat Rev Genet*, **18**, 164-179.

103. Nakahata, Y., Kaluzova, M., Grimaldi, B., Sahar, S., Hirayama, J., Chen, D., Guarente, L.P. and Sassone-Corsi, P. (2008) The NAD⁺-Dependent Deacetylase SIRT1 Modulates CLOCK-Mediated Chromatin Remodeling and Circadian Control. *Cell*, **134**, 329-340.

104. Aguilar-Arnal, L. and Sassone-Corsi, P. (2015) Chromatin landscape and circadian dynamics: Spatial and temporal organization of clock transcription. *Proceedings of the National Academy of Sciences*, **112**, 6863-6870.

105. Doi, M., Hirayama, J. and Sassone-Corsi, P. (2006) Circadian Regulator CLOCK Is a Histone Acetyltransferase. *Cell*, **125**, 497-508.

106. Stashi, E., Lanz, R.B., Mao, J., Michailidis, G., Zhu, B., Kettner, N.M., Putluri, N., Reineke, E.L., Reineke, L.C. and Dasgupta, S. (2014) SRC-2 is an essential coactivator for orchestrating metabolism and circadian rhythm. *Cell reports*, **6**, 633-645.

107. Feng, D., Liu, T., Sun, Z., Bugge, A., Mullican, S.E., Alenghat, T., Liu, X.S. and Lazar, M.A. (2011) A circadian rhythm orchestrated by histone deacetylase 3 controls hepatic lipid metabolism. *Science*, **331**, 1315-1319.

108. Alenghat, T., Meyers, K., Mullican, S.E., Leitner, K., Adeniji-Adele, A., Avila, J., Bućan, M., Ahima, R.S., Kaestner, K.H. and Lazar, M.A. (2008) Nuclear receptor corepressor and histone deacetylase 3 govern circadian metabolic physiology. *Nature*, **456**, 997-1000.

109. Chen, Y.C., Koutelou, E. and Dent, S.Y.R. (2022) Now open: Evolving insights to the roles of lysine acetylation in chromatin organization and function. *Mol Cell*, **82**, 716-727.

110. Policarpi, C., Munafò, M., Tsagkris, S., Carlini, V. and Hackett, J.A. (2024) Systematic epigenome editing captures the context-dependent instructive function of chromatin modifications. *Nature Genetics*, **56**, 1168-1180.

111. Mazina, M.Y., Nikolenko, Y.V., Krasnov, A.N. and Vorobyeva, N.E. (2016) SWI/SNF protein complexes participate in the initiation and elongation stages of Drosophila hsp70 gene transcription. *Russian Journal of Genetics*, **52**, 141-145.

112. Schwabish, M.A. and Struhl, K. (2007) The Swi/Snf complex is important for histone eviction during transcriptional activation and RNA polymerase II elongation in vivo. *Mol Cell Biol*, **27**, 6987-6995.

113. Huang, Y., Jay, K.L., Huang, A.Y.-W., Wan, J., Jangam, S.V., Chorin, O., Rothschild, A., Barel, O., Mariani, M., Iascone, M. *et al.* Loss-of-function in RBBP5 results in a syndromic neurodevelopmental disorder associated with microcephaly. *Genetics in Medicine*.

Fig. legends

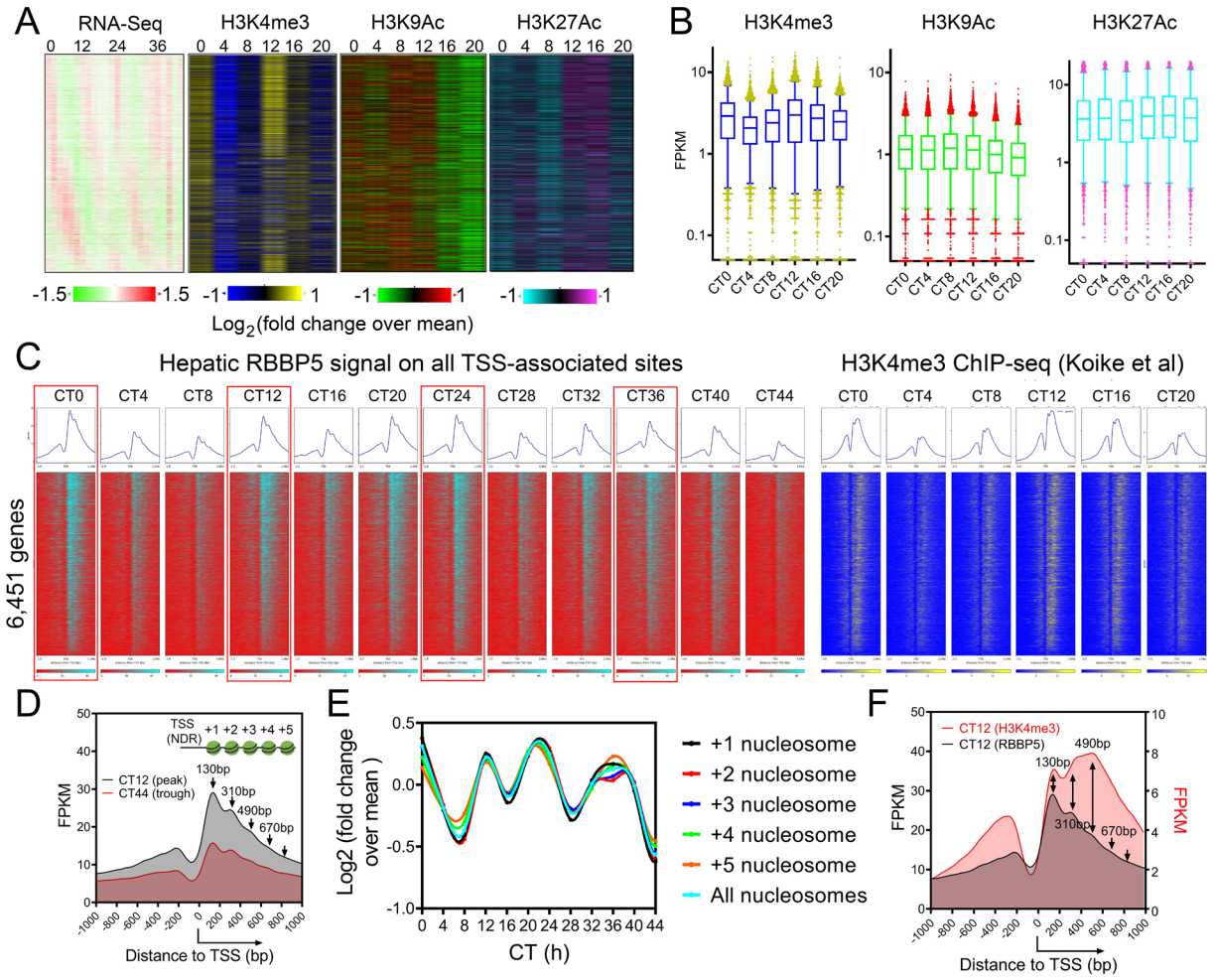

Fig. 1. Global ~12h RBBP5 cistrome is associated with promoter-proximal ~12h H3K4me3 epigenome in mouse liver. (A) Heatmap of ~12h hepatic transcriptome aligned with H3K4me3, H3K9Ac and H3K27Ac cistromes. **(B)** Quantification of temporal H3K4me3, H3K9ac and H3K27Ac. **(C)** Heatmap showing RBBP5 and H3K4me3 chromatin occupancy 1kb ± of TSS of 6,451 genes. **(D)** RBBP5 chromatin occupancy aligned with nucleosome positioning. **(E)** Quantification of temporal average RBBP5 binding intensity on different nucleosomes. **(F)** RBBP5 chromatin occupancy aligned with H3K4me3 occupancy.

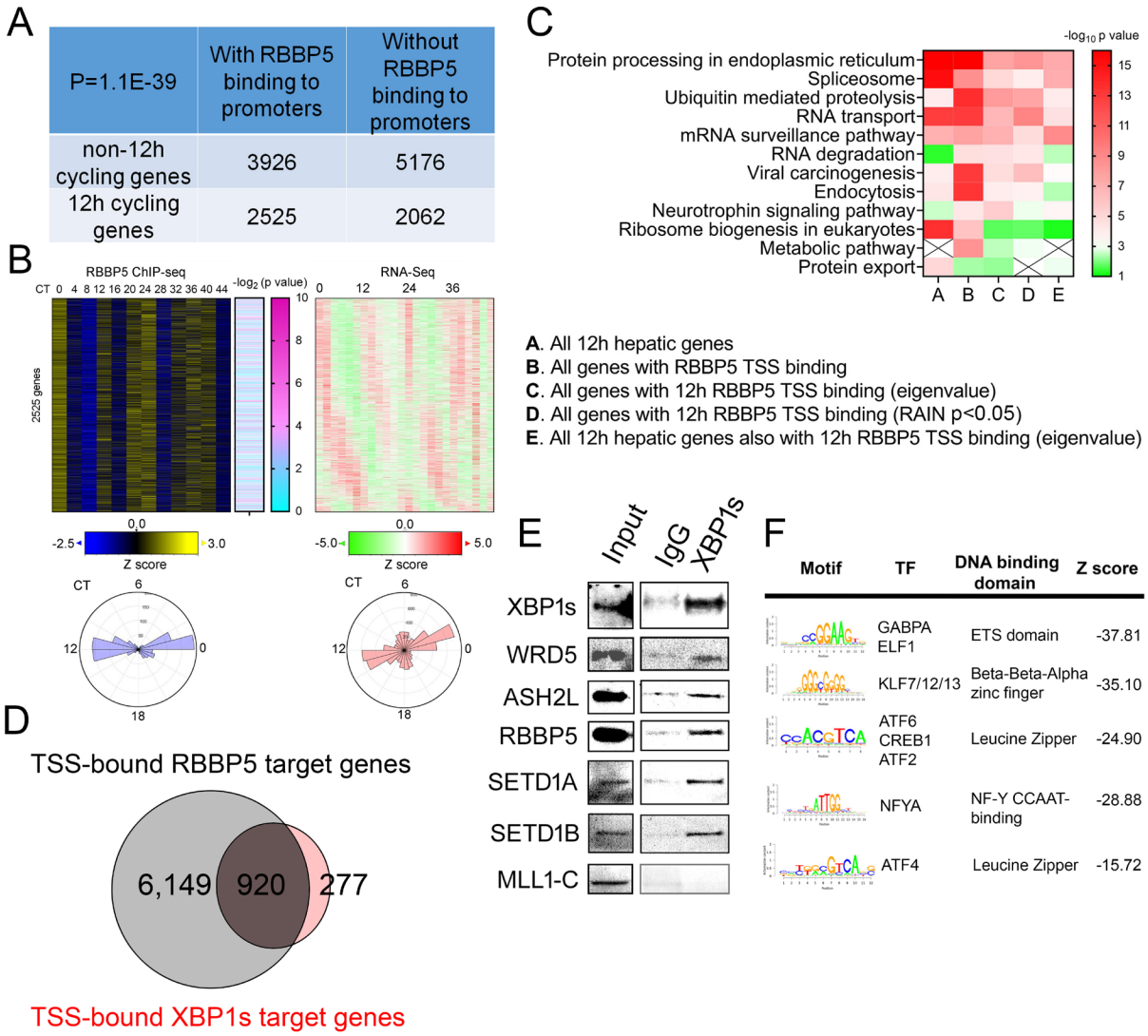

Fig. 2. Hepatic RBBP5 cistrome coincides with that of XBP1s and hepatic ~12h transcriptome. (A) The table shows the number of genes with or without ~12h rhythms and with or without promoter RBBP5 binding. **(B)** Heatmap showing RBBP5 binding intensity along with -$\log_{10}$ transformed P values for having 1~2h rhythm by RAIN and ~12h rhythms of gene expression on 2,525 genes. **(C)** Heat map summary of GO analysis demonstrating the -$\log_{10}$ transformed P value of different enriched pathways for different genes. **(D)** Venn diagram demonstrating distinct and common cistromes for RBBP5 and XBP1s. **(E)** Western blot showing co-IP in liver nuclear extracts from CT0 using anti-XBP1s and normal IgG control antibody. **(F)** Motif analysis of RBBP5 binding sites of 6,149 genes.

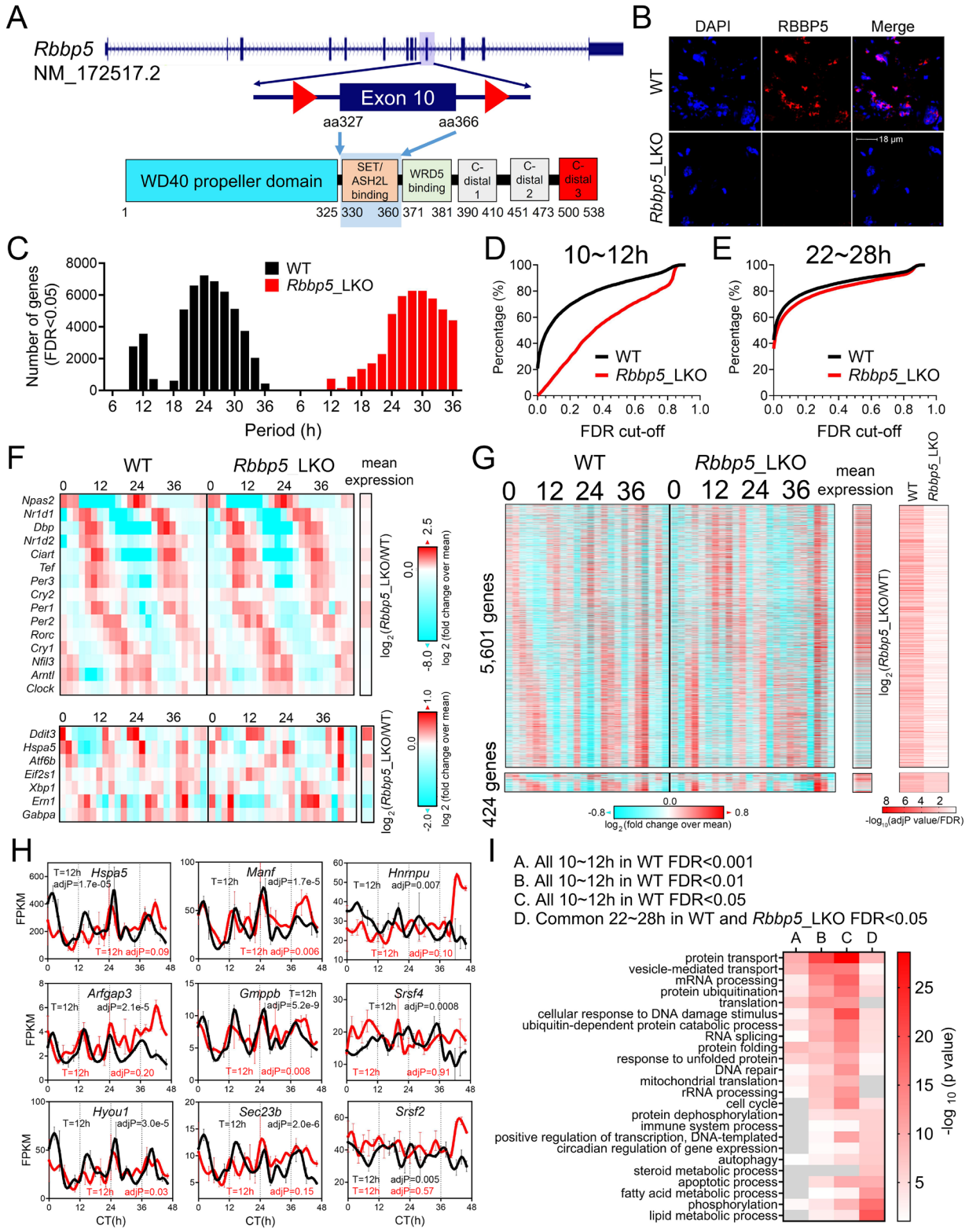

Fig. 3. RBBP5 is an epigenetic regulator of the hepatic ~12h oscillator, but not the canonical ~24h circadian clock. (A) Schematic of the design of *Rbbp5*^{Flox} mice. **(B)**

Immunofluorescence of RBBP5 in the liver of *Rbbp5* ^{Flox} and *Rbbp5* ^{LKO} mice. **(C)** Histograms showing the period distributions of all rhythmic genes uncovered from *Rbbp5* ^{Flox} and *Rbbp5* ^{LKO} mice (with adjP values or FDR <0.05) (n=2 at each time point for either genotype). **(D, E)** Cumulative distribution of 10~12h **(D)** and 22~28h **(E)** genes in *Rbbp5* ^{Flox} and *Rbbp5* ^{LKO} mice with different FDR cut-offs. **(F)** Heat map of 15 core circadian clock (top) and canonical ~12h gene expression (bottom) in the liver of *Rbbp5* ^{Flox} and *Rbbp5* ^{LKO} mice. Log_2 normalized fold change of average gene expression across 48 hours between *Rbbp5* ^{Flox} and *Rbbp5* ^{LKO} mice was also shown. **(G)** Heat map of 6,025 ~12h gene expression (FDR<0.05) in the liver of *Rbbp5* ^{Flox} and *Rbbp5* ^{LKO} mice, with 5,601 of them lost in *Rbbp5* ^{LKO} mice, along with $-log_{10}$ transformed adjP values for having 10-12h rhythm by RAIN. Log_2 normalized fold change of average gene expression across 48 hours between *Rbbp5* ^{Flox} and *Rbbp5* ^{LKO} mice was also shown. **(H)** RNA-Seq data for representative proteostasis and mRNA processing genes in the liver of *Rbbp5* ^{Flox} and *Rbbp5* ^{LKO} mice. **(I)** Heat map summary of GO analysis demonstrating the $-log_{10}$ transformed P values of different enriched pathways for different genes. Data: Mean ± S.E.M.

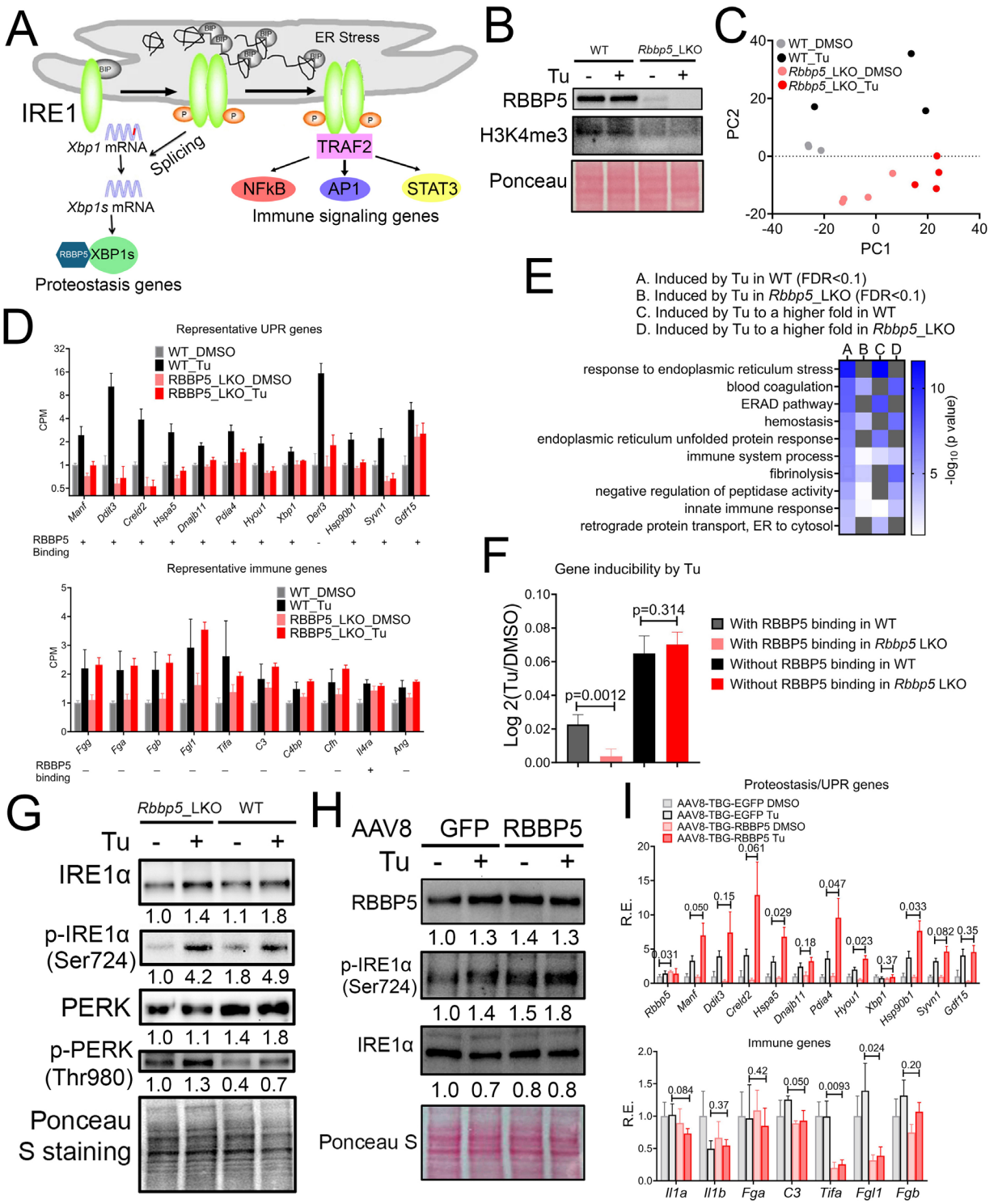

Fig. 4. RBBP5 regulates the hepatic transcriptional response to proteotoxic stress. (A) The diagram of UPR. **(B)** Western blot analysis in the liver of *Rbbp5* ^{Flox} and *Rbbp5* ^{LKO} mice with or without Tu treatment. **(C)** PCA showing the hepatic transcriptional response to Tu in *Rbbp5* ^{Flox} and *Rbbp5* ^{LKO} mice. **(D)** Representative RNA-seq data for proteostasis (top) and immune genes (bottom) with RBBP5 promoter-binding status also shown below. n=3 for *Rbbp5* ^{Flox} DMSO and

1355 *Rbbp5* ^{Flox} Tu, and n=4 for *Rbbp5* ^{LKO} DMSO and *Rbbp5* ^{LKO} Tu. **(E)** Heat map summary of GO
1356 analysis demonstrating the -$\log_{10}$ transformed P values of different enriched pathways for different
1357 genes. **(F)** Log $_2$ normalized fold induction by Tu in *Rbbp5* ^{Flox} and *Rbbp5* ^{LKO} mice for genes with
1358 or without RBBP5 promoter binding. **(G)** Western blot analysis of different proteins in *Rbbp5* ^{Flox}
1359 and *Rbbp5* ^{LKO} mice treated with or without Tu. **(H, I)** Mice tail-vein injected with AAV8-TGB-GFP
1360 or AAV8-TGB-RBBP5 were treated with or without Tu. Western blot analysis **(H)** and qPCR **(I)**.
1361 n=3 for AAV8-TBG-EGFP DMSO, n=4 for AAV8-TBG-EGFP Tu, n=4 for AAV8-TGB-mRBBP5
1362 DMSO and n=4 for AAV8-TGB-mRBBP5 Tu. Data: Mean ± S.E.M.

1363

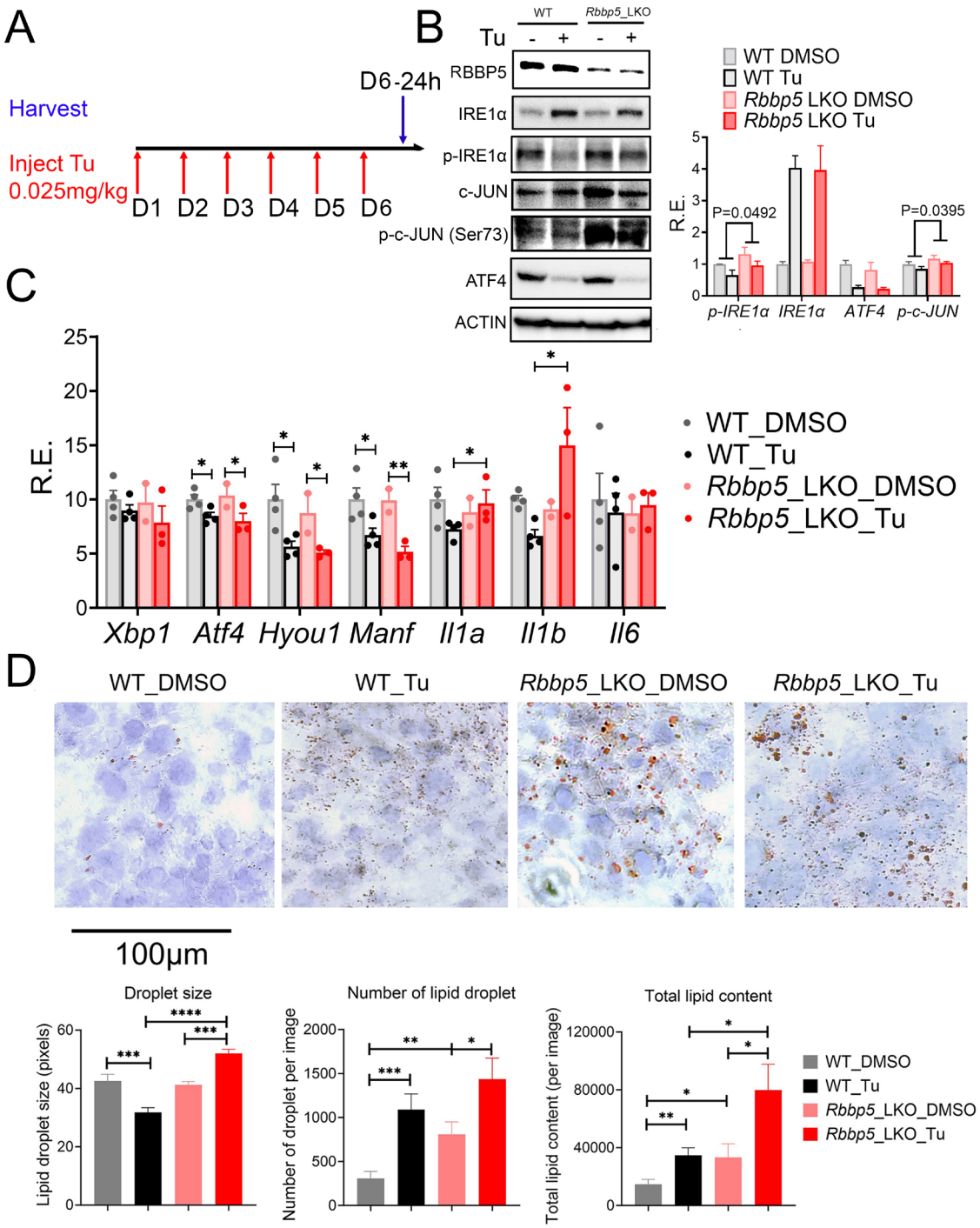

Fig. 5. RBBP5 protects mice from chronic ER stress-induced hepatic inflammation and steatosis. (A) A schematic of experimental design. **(B)** Western blot and quantification of the expression of different proteins in *Rbbp5* ^{Flox} and *Rbbp5* ^{LKO} mice with or without repeated Tu injection. **(C)** qPCR analysis of different proteostasis and immune gene expressions in the same cohort of mice. **(D)** Representative images of Oil Red O staining and quantification of lipid droplet size, number and total lipid content (total lipid droplet area). n=4 for *Rbbp5* ^{Flox} DMSO, n=4 for *Rbbp5* ^{Flox} Tu, n=2 for *Rbbp5* ^{LKO} DMSO, n=3 for *Rbbp5* ^{LKO} Tu. Data: Mean ± S.E.M.

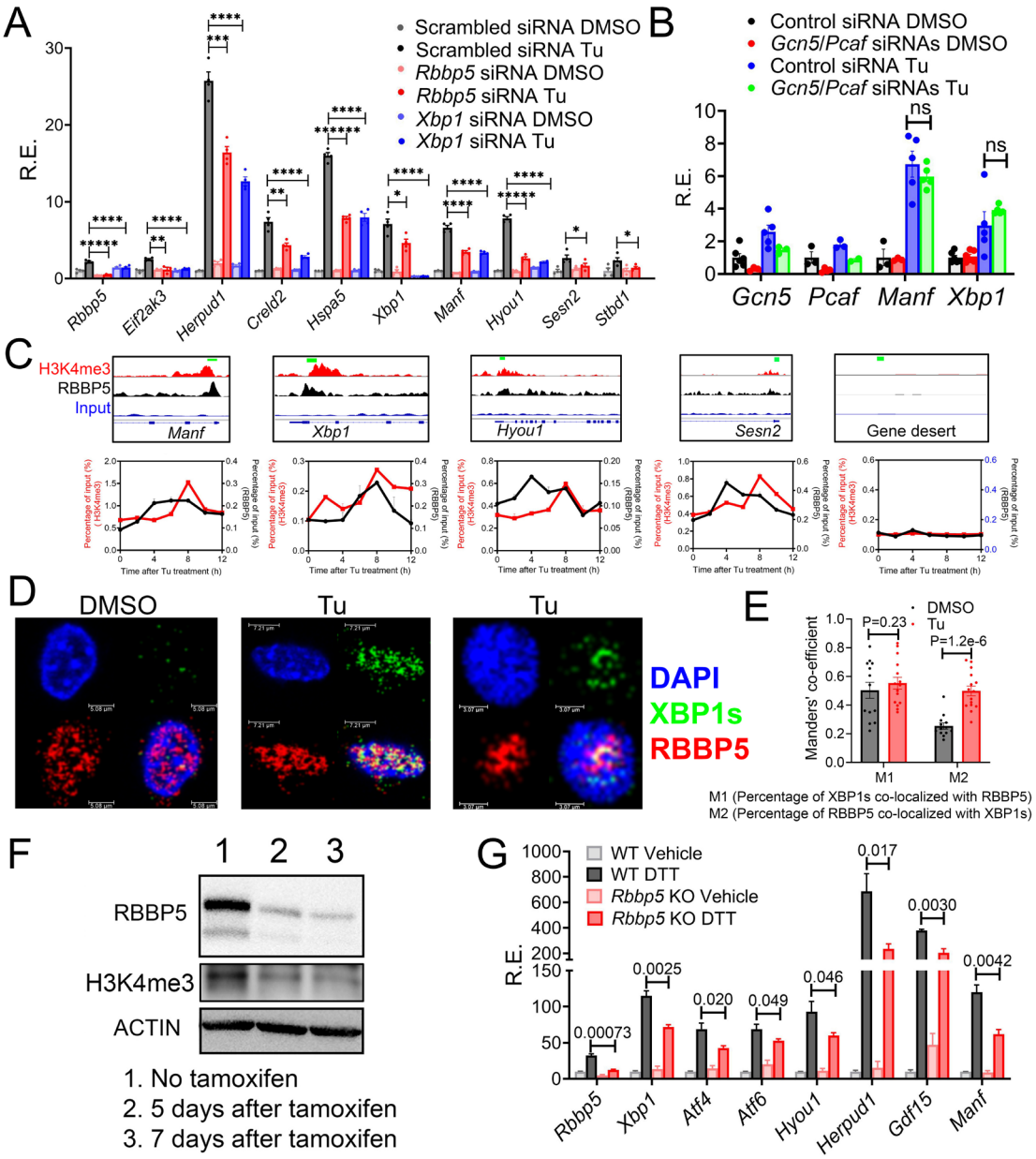

Fig. 6. RBBP5 is required for cell-autonomous transcriptional response to ER stress. (A) qPCR of different genes in MEFs transfected with scrambled, *Rbbp5* or *Xbp1* siRNAs and treated with DMSO or Tu (100ng/ml) for 8 hours. **(B)** qPCR of different genes in MEFs transfected with scrambled, or the combination *Gcn5* and *Pcaf* siRNAs and treated with DMSO or Tu (100ng/ml) for 8 hours. (**C**) Selected genes aligned for RBBP5 and H3K4me3 ChIP-seq signal from CT0 mouse liver and ChIP-qPCR of RBBP5 and H3K4me3 in MEFs treated with Tu for different hours. (**D, E**) Immunofluorescence of XBP1s and RBBP5 in MEFs treated with vehicle control (DMSO) or Tu (100ng/ml) for 8 hours (**D**) and quantification of Manders' coefficient of colocalization of XBP1s with RBBP5 (**E**). (**F**) *Rbbp5* (fl/fl) ROSA26-CreERT2 (+/+) MEFs were treated with tamoxifen for 5 or 7 days and western blot analysis was performed. (**G**) qPCR of different genes in *Rbbp5* (fl/fl) ROSA26-CreERT2 (+/+) MEFs treated with vehicle (WT) or tamoxifen (*Rbbp5* KO) followed by treatment with vehicle control or 1mM DTT for 5 hours. Data: Mean ± S.E.M.

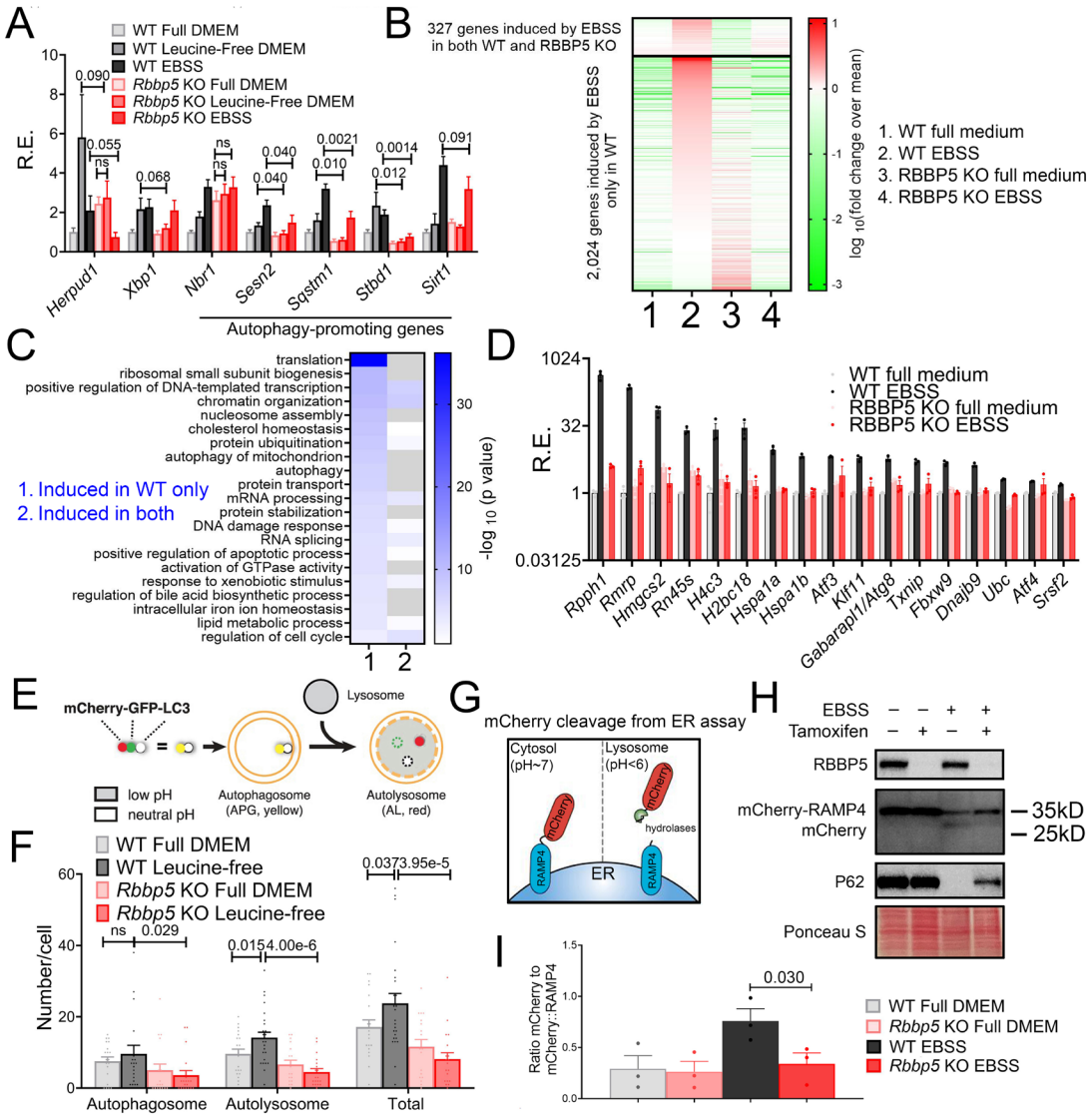

Fig. 7. RBBP5 is required for cell-autonomous transcriptional response to nutrient deprivation. (A) qPCR analysis of *Rbbp5* (fl/fl) ROSA26-CreERT2 (+/+) MEFs pre-treated with (RBBP5 KO) or without (WT) tamoxifen and then treated with full DMEM media, leucine-free media or EBSS for 16 hours. **(B-D)**. Transcriptome profiling of *Rbbp5* (fl/fl) ROSA26-CreERT2 (+/+) MEFs pre-treated with (RBBP5 KO) or without (WT) tamoxifen and then treated with full DMEM media or EBSS for 16 hours by RNA-seq. Heatmap of all genes that are induced by EBSS in WT cells by EBSS (adjP<0.05) (**B**). GO analysis of EBSS-induced genes in only WT or both genotypes (**C**), and representative gene expression (**D**). **(E)** Diagram of the mCherry-GFP-LC3 autophagy reporter. **(F)** Quantification of autophagic flux in mCherry-GFP-LC3-expressing *Rbbp5* (fl/fl) ROSA26-CreERT2 (+/+) MEFs treated with vehicle (WT) or tamoxifen (*Rbbp5* KO) followed by treatment with full DMEM media or leucine-free media for 16 hours. **(G)** Diagram of the ER-phagy reporter using the mCherry cleavage from ER assay. **(H, I)** Western blot of different proteins **(H)** and quantification **(I)** of mCherry cleavage in RAMP4-mCherry-expressing *Rbbp5* (fl/fl) ROSA26-CreERT2 (+/+) MEFs treated with vehicle (WT) or tamoxifen (*Rbbp5* KO) followed by treatment with full DMEM media or EBSS for 16 hours. Data: Mean ± S.E.M.

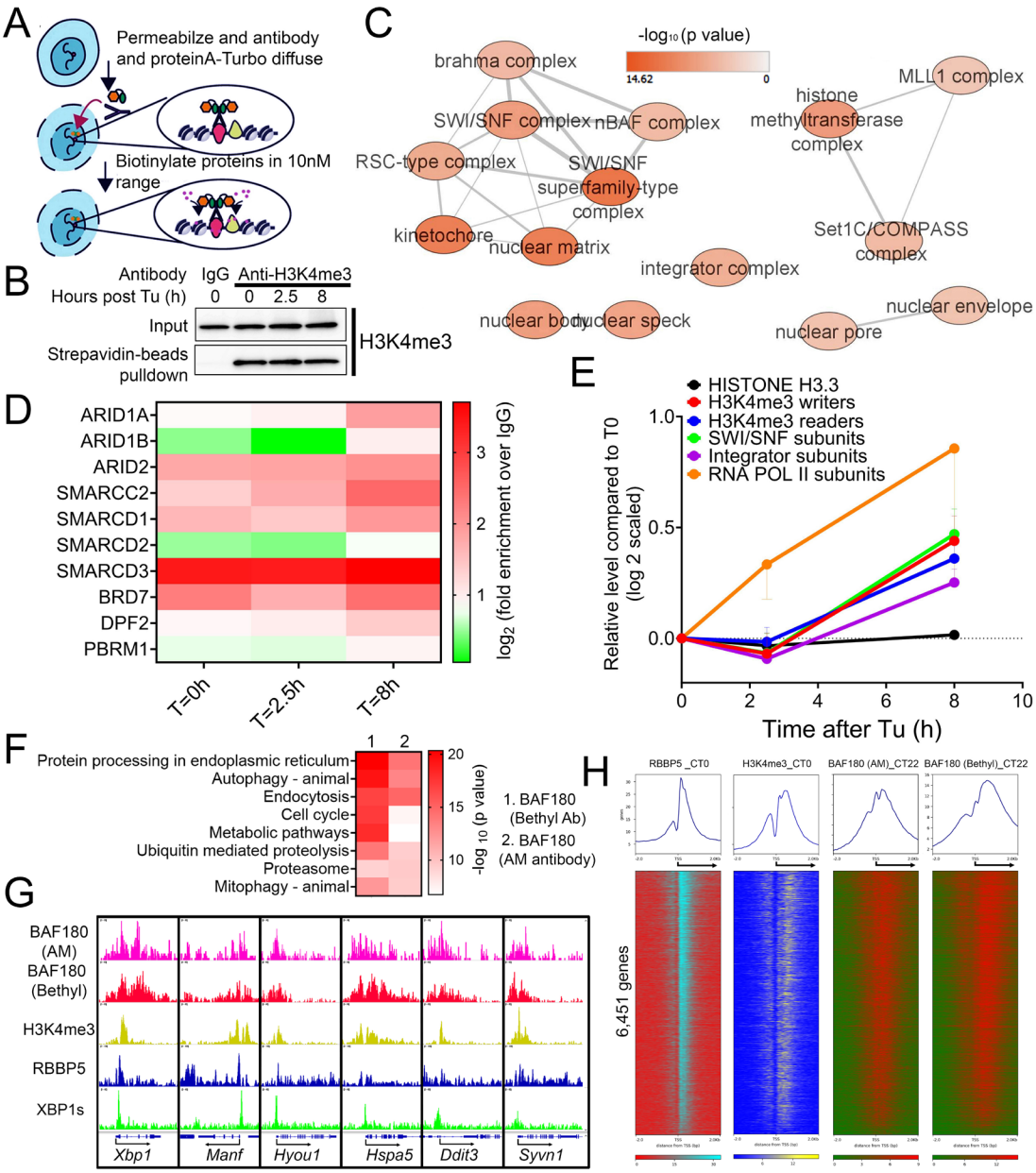

Fig. 8. Proximity labeling reveals H3K4me-associated proteomic architecture of the proteostatic stress response. (**A**) A diagram illustrating the procedure of performing H3K4me3 proximity labeling via using the recombinant Protein A-TurboID. (**B**) Western blot analysis showing the nuclear level of total (input) or biotinylated (after streptavidin beads pull-down) level of H3K4me3 in MEF treated with 100ng/ml Tu for 0, 2.5 or 8h before subject to anti-IgG and anti-H3K4me3 antibody-based proximity labeling. (**C**) Enriched biological network of 239 proteins. (**D**) Heatmap of fold enrichment of different SWI/SNF subunits (over IgG control) at different times after ER stress. (**E**) Quantification of the average relative enrichment of proteins in different complexes at different times after ER stress. (**F**) GO analysis of BAF180 hepatic cistrome. (**G**) Selected UPR genes aligned for BAF180, RBBP5, H3K4me3 and XBP1s ChIP-seq signal in mouse liver. (**H**) Heatmap showing RBBP5, H3K4me3 and BAF180 chromatin occupancy 2kb ± of TSS of 6,451 genes. Data: Mean ± S.E.M.

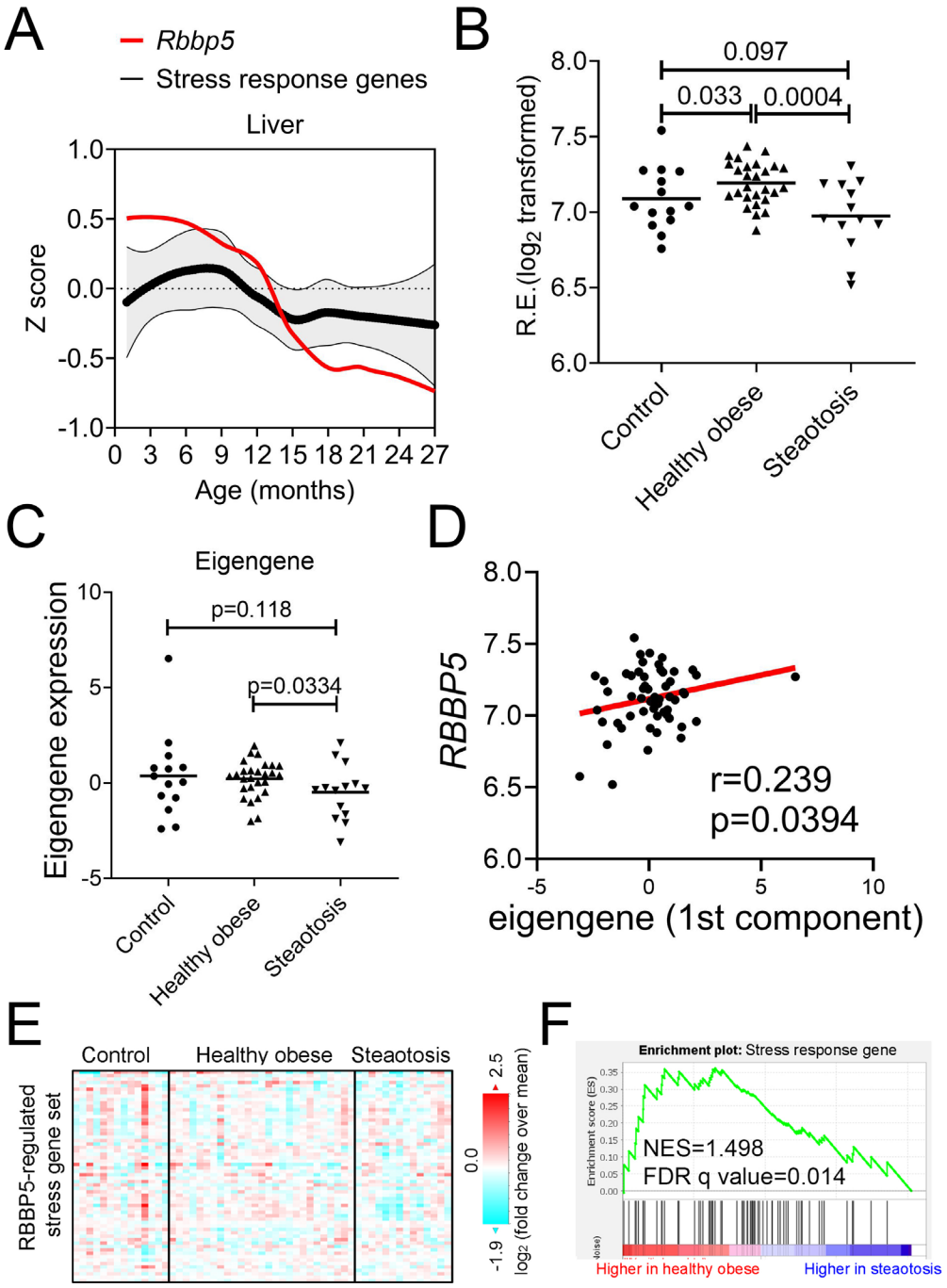

Fig. 9. Reduced RBBP5 expression is associated with aging in mice and hepatic steatosis in humans. (A) Z score-normalized expression of mouse *Rbbp5* and average expression of stress response genes across mouse life span according to Tabua Muris dataset (97). **(B-F)** Data in humans with NAFLD/MAFLD was from (99). Expression of *RBBP5* (**B**) and the eigengene of 97 stress genes (**C**). (**D**) Scatter plot showing a positive correlation between *RBBP5* and eigengene expression. **(E)** Heatmap of 97 stress genes expression in different cohorts of human subjects. (**F**) GSEA analysis showing stress gene expression are downregulated in steatosis subjects.